

Reverse micelle strategy for effective substitutional Fe-doping in small-sized CeO₂ nanocrystals:
Assessment of adsorption and photodegradation efficiency of ibuprofen under

Original

Reverse micelle strategy for effective substitutional Fe-doping in small-sized CeO₂ nanocrystals: Assessment of adsorption and photodegradation efficiency of ibuprofen under visible light / Tammaro, Olimpia; Paparo, Rosanna; Chianese, Marica; Ritacco, Ida; Caporaso, Lucia; Camellone, Matteo Farnesi; Masenelli, Bruno; Lamirand, Anne D.; Bluet, Jean-Marie; Fontana, Marco; Pinto, Gabriella; Illiano, Anna; Amoresano, Angela; Serio, Martino Di; Russo, Vincenzo; Esposito, Serena. - In: CHEMICAL ENGINEERING JOURNAL. - ISSN 1385-8947. - 479:(2024).

[10.1016/j.cej.2023.147909]

Availability:

This version is available at: 11583/2984584 since: 2023-12-18T10:18:43Z

Publisher:

Elsevier

Published

DOI:10.1016/j.cej.2023.147909

Terms of use:

This article is made available under terms and conditions as specified in the corresponding bibliographic description in the repository

Publisher copyright

(Article begins on next page)

Journal Pre-proofs

Reverse micelle strategy for effective substitutional Fe-doping in small-sized CeO₂ nanocrystals: Assessment of adsorption and photodegradation efficiency of ibuprofen under visible light

Olimpia Tammamaro, Rosanna Paparo, Marica Chianese, Ida Ritacco, Lucia Caporaso, Matteo Farnesi Camellone, Bruno Masenelli, Anne D. Lamirand, Jean-Marie Bluet, Marco Fontana, Gabriella Pinto, Anna Illiano, Angela Amoresano, Martino Di Serio, Vincenzo Russo, Serena Esposito

PII: S1385-8947(23)06641-X
DOI: <https://doi.org/10.1016/j.cej.2023.147909>
Reference: CEJ 147909

To appear in: *Chemical Engineering Journal*

Received Date: 18 August 2023
Revised Date: 22 November 2023
Accepted Date: 4 December 2023

Please cite this article as: O. Tammamaro, R. Paparo, M. Chianese, I. Ritacco, L. Caporaso, M.F. Camellone, B. Masenelli, A.D. Lamirand, J-M. Bluet, M. Fontana, G. Pinto, A. Illiano, A. Amoresano, M.D. Serio, V. Russo, S. Esposito, Reverse micelle strategy for effective substitutional Fe-doping in small-sized CeO₂ nanocrystals: Assessment of adsorption and photodegradation efficiency of ibuprofen under visible light, *Chemical Engineering Journal* (2023), doi: <https://doi.org/10.1016/j.cej.2023.147909>

This is a PDF file of an article that has undergone enhancements after acceptance, such as the addition of a cover page and metadata, and formatting for readability, but it is not yet the definitive version of record. This version will undergo additional copyediting, typesetting and review before it is published in its final form, but we are providing this version to give early visibility of the article. Please note that, during the production process, errors may be discovered which could affect the content, and all legal disclaimers that apply to the journal pertain.

© 2023 The Author(s). Published by Elsevier B.V.



Reverse micelle strategy for effective substitutional Fe-doping in small-sized CeO₂ nanocrystals: assessment of adsorption and photodegradation efficiency of ibuprofen under visible light

Olimpia Tammaro^{1,2}, Rosanna Paparo³, Marica Chianese³, Ida Ritacco⁴, Lucia Caporaso⁴, Matteo Farnesi Camellone⁵, Bruno Masenelli⁶, Anne D. Lamirand⁶, Jean-Marie Bluet⁶, Marco Fontana^{1,7}, Gabriella Pinto³, Anna Illiano³, Angela Amoresano³, Martino Di Serio³, Vincenzo Russo^{3*}, Serena Esposito^{1,2*}

¹ Department of Applied Science and Technology and INSTM Unit of Torino – Politecnico, Politecnico di Torino, Corso Duca degli Abruzzi 24, 10129, Torino, Italy

² PoliTO BioMED Interdepartmental LAB, Corso Duca degli Abruzzi 24, 10129 Torino, Italy

³ University of Naples “Federico II”, Department of Chemical Sciences, Complesso Universitario Monte S. Angelo, Via Cintia 4, IT 80126 Naples, Italy

⁴ Dipartimento di Chimica e Biologia, Università degli Studi di Salerno, via Giovanni Paolo II 132, 84084 Fisciano, Salerno, Italy

⁵ Consiglio Nazionale delle Ricerche-Istituto Officina dei Materiali (CNR-IOM), 34136 Trieste, Italy

⁶ University of Lyon, INSA Lyon, ECL, CNRS, UCBL, CPE Lyon, INL, UMR5270, 69621 Villeurbanne, France.

⁷ Center for Sustainable Future Technologies @POLITO, Istituto Italiano di Tecnologia, Via Livorno 60, Turin 10144, Italy

Corresponding authors: serena_esposito@polito.it; v.russo@unina.it

Abstract

Reverse micelle nanoreactors were successfully designed to synthesize small-sized ceria nanocrystals (3.5-4.2 nm) with a sizeable amount of substitutional iron. Undoped and doped CeO₂ catalysts with an iron content (0.50-10 mol %) compliant with the nominal value were prepared and tested for the first time for the removal of ibuprofen both in the dark and under UV or visible light irradiation.

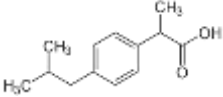
The effective inclusion and distribution of iron in the ceria lattice were ascertained through in-depth physicochemical characterization. In particular, X-ray diffraction suggested the formation of an F-type crystal structure, ruling out the formation of separate iron-containing crystalline phases. On the other hand, substitutional doping of CeO₂ with Fe atoms favoured the formation of Ce³⁺ defects and vacancy sites (VOs) with a maximum for the sample with 2.5 mol % iron (Fe2.5), as evidenced by X-ray photoelectron spectroscopy (XPS) measurements and Raman spectroscopy. UV-Vis spectroscopy showed that the optical properties were successfully modified by the presence of iron, which causes a gradual decrease in band gap as iron content increases. The experimental evidence was further verified and supported by density functional theory calculations. DFT calculations also revealed that the surface iron and oxygen vacancies are the preferential sites for ibuprofen adsorption. Nevertheless, it was found under dark conditions that adsorption capacity does not monotonically increase with iron content, revealing contrasting roles of surface characteristics. Indeed, catalytic experiments have identified a trade-off between adsorption and photodegradation, identifying Fe2.5 as the best-performing catalyst for ibuprofen removal under visible light irradiation. These results were discussed by considering the key properties of the catalysts as well as their different surface charge determined by ζ potential measurements. The best catalyst was tested through reuse experiments that proved its stability over 4 cycles. Finally, an attempt was made to identify the photodegradation by-products, allowing the detection of 1-ethenyl-4-(2-methylpropyl)benzene as the main by-product.

Keywords: Substitutional Fe doped CeO₂, Reverse micelle, Ibuprofen, Photodegradation, DFT.

1. Introduction

Pharmaceuticals are considered emerging environmental pollutants due to the increase in their consumption and consequent accumulation in water [1]. Ibuprofen (IBU) (Table 1), is among the most widespread non-steroidal anti-inflammatory drugs (NSAIDs) in the world, whose presence in wastewater is a serious concern because it is not biodegradable [2]. The detected concentrations for ibuprofen in wastewater treatment plants are in the ranges of 55–69 $\mu\text{g}\cdot\text{L}^{-1}$ [3]. Over the last few years, to address this environmental concern, several chemical, physical and biological methods have been proposed [4]. Chemical methods include advanced oxidation processes (AOPs), coagulation-flocculation, electrocoagulation, chemical oxidation, and ion exchange [4]. Among those, AOPs can degrade recalcitrant pollutants with a rapid reaction rate and high removal efficiency due to the generation of reactive free radicals [5].

Table 1 - Structure and properties of ibuprofen

Compound	IUPAC name	Molecular formula	Molecular weight	Solubility in water	Structure
IBU	2-[4-(2-methyl propyl) phenyl]propanoic acid	$\text{C}_{13}\text{H}_{18}\text{O}_2$	206.28 g/mol	21 mg/L (at 25 °C)	

The use of semiconductors has broadened AOPs to heterogeneous photocatalysis, a process operating at room temperature and atmospheric pressure [5–8]. Moreover, the combination, through the design of an appropriate catalyst, with solar reactors makes this method stand out from others in terms of environmental friendliness and cost-effectiveness through the use of renewable energy [9–11]. Indeed, nowadays, new photocatalysts active in the visible range are attracting increasing interest among the scientific community [9].

Although some formulations for the catalytic photodegradation of ibuprofen under visible light were explored, the proposed solutions suffer from the complicated design of the photocatalyst [12–17], and typically the experiments are conducted in harsh reaction conditions (e.g., powerful lamps, highly concentrated systems [14,15]). The challenge is therefore to design simple, inexpensive, high-performance catalysts for optimal degradation of ibuprofen under visible light irradiation.

Cerium oxide was selected for its many trade-offs between reactivity, photochemical stability, cost-effectiveness, and the environmentally friendly nature of CeO_2 nanoparticles (CeO_2 -NPs) [18–21].

The photocatalytic activity of cerium oxide can be enhanced, increasing the photo-absorption capability, by replacing a small fraction of Ce^{4+} with a different cation [22,23]. Among heteroatom dopants, transition metals are particularly appealing as they can create defect states in the band gap or introduce energy levels into it. In this regard, iron is considered one of the most attractive candidates on account of its environmental compatibility, abundance, and low cost [24]. One of the most intriguing features of using Fe^{3+} as a dopant is the possibility of further promoting the generation of oxygen vacancies (VOs) and the reversible conversion between the $\text{Ce}^{4+}/\text{Ce}^{3+}$ valence state. [25,26]. Oxygen vacancies not only extend the absorption edge but are reported to delay the electron–

hole recombination rates, thus increasing the separation efficiency of carriers for enhanced photocatalytic performances [27,28].

In conclusion, the introduction of Fe trivalent ions can be considered a powerful tool for rational defect engineering. Indeed, the beneficial effect of iron doping is reported by a certain number of papers for the photodegradation of model dye molecules under visible irradiation, recently reviewed [22]. Nevertheless, it must be considered that the influence of metal dopant and VOs on the ceria properties is interrelated to the concentration, distribution or position of Fe and defects in the ceria lattice [29]. In particular, the extent to which these features occur can be strongly impacted by the preparation method [30].

In this scenario, it should be noted that many methods reported in the literature suffer from poor reproducibility and control of process parameters, often failing to achieve real doping or, on the other hand, requiring harsh operating conditions [31–36]. The hydrothermal method was exploited by Cai et al. [32] for preparing Fe-doped ceria materials with different doping amounts. They obtained a catalyst with a crystallite size of approximately 100 Å and observed that the low Fe³⁺ doping could effectively improve the concentration of Ce³⁺, enhancing the degradation ability of the model dye Acid Orange 7 (AO7). However, despite the versatility of the hydrothermal approach, it still represents a “black box” method as is impossible to have strict control over the process. Channei et al. [36] used flame pyrolysis to produce photocatalysts based on Fe-doped CeO₂ nanoparticles for the conversion of both formic acid and oxalic acid. This method, such as the aforementioned hydrothermal method, does not easily allow the control and variation of synthesis parameters invalidating the simplicity of the experimental setup [37].

In this perspective, it is important to have a method that goes beyond the trial-and-error approach and allows rigorous control of the composition of the catalyst, preserving its homogeneity and promoting improved optical, structural, and morphological properties.

Based on the previous considerations, in our work, we bring the reader's attention to a Fe-doped ceria system, so far never adopted for the photodegradation of ibuprofen. A further outcome of this research was the development of a versatile and reliable synthesis protocol, capable of exploiting the recognised advantages and potential of the one-pot reverse micelle approach. From a practical point of view, a significant advantage of the method is its scalability, including synthesis in microfluidic systems, for the production of larger quantities of catalysts [38–44].

The homogeneity of the final material is due to atomic-scale mixing, which in turn is ensured by the presence of a small aqueous core, where the reaction takes place. This mixing allows to easily promote the presence of the dopant in the oxide lattice. The size and shape of these small water domains can be controlled by varying the ratio between the liquid phases (water and oil) and selecting the right surfactant in terms of both type (non-ionic, anionic, cationic and amphoteric) and amount. As a result, not only the intimate contact of the metal precursor is well confined, but also the relative nucleation on growth steps can be easily monitored [45].

A pure ceria and iron-doped ceria with metal contents of 0.5, 2.5, 5 and 10 mol % Fe were prepared channelling the reactions that usually take place in aqueous media into the small domains of the reverse micelles.

To assess the physicochemical properties and to understand the structure/composition-activity relationship of Fe-doped CeO₂ in the photodegradation of ibuprofen, an in-depth characterisation was conducted. In detail, the prepared catalysts were characterised using various analytical techniques such as inductively coupled plasma mass spectrometry (ICP-MS), Thermogravimetric analysis (TGA), X-ray diffraction (XRD), high-resolution transmission electron microscopy (HR-TEM), Field

emission scanning electron microscopy (FESEM), Diffuse reflectance spectroscopy (DR/UV-Vis), Raman spectroscopy, N₂ adsorption/desorption at -196 °C, X-ray photoelectron spectroscopy (XPS) and ζ -potential measurements.

Density Functional Theory (DFT) calculations were performed in order to investigate the stability and the effects on the electronic and structural properties of the CeO₂(111) in the presence of substitutional and interstitial Fe atoms. The calculations suggest that, in a wide range of temperatures and pressure, the thermodynamically most stable structures are the ones where Fe atoms substitute Ce sites in the presence or absence of oxygen vacancies in agreement with the experimental observations. Additional calculations were performed to investigate the interaction between undoped and Fe-doped ceria surfaces with ibuprofen in order to identify preferential sites for adsorption.

The catalysts were tested both in the dark and under either UV or visible irradiation, to compare the performance of each synthesized material. A preliminary kinetic model was implemented to measure the activity of each catalyst in terms of both ibuprofen adsorption and related photodegradation. Reuse experiments were conducted to test the stability of the most active material, further assessed by post-reaction characterizations. Finally, an attempt was made to determine the photodegradation products via specific analytical methods (i.e., GC and LC-MS).

2. Materials and methods

Cyclohexane (ACS reagent $\geq 99.5\%$), cerium nitrate hexahydrate, iron chloride (reagent grade 97%), ammonia (ACS reagent 28-30%), 1-butanol (ACS reagent $\geq 99.4\%$), polyoxyethylene (10) cetyl ether (Brij C10) and ethanol (puriss $\geq 99.8\%$) were purchased by Sigma-Aldrich and used without further modification. Bi-distilled water has been used for the preparation of salt solution. Ibuprofen solutions were prepared using 4-isobutyl- α -methylphenylacetic acid, 99% (manufactured by Alfa Aesar).

2.1 Precipitation by reverse micelles

In a typical synthesis, adapted from the literature [46,47], the oil/surfactant phase is prepared by dissolving 8.2 g of surfactant (Brij C10) in 100 mL of cyclohexane under stirring at room temperature. An aqueous solution is prepared by dissolving the proper amount of cerium and iron precursors in distillate water to achieve a final concentration of 0.5M. The volume of the aqueous precursor solution has been selected to obtain a w_0 value of 25 (w_0 is defined as the water-surfactant molar ratio). The aqueous solution is slowly added dropwise to the oil phase to obtain appropriate water-in-oil (w/o) micelles. To preserve the optical transparency of the emulsion, avoiding the formation of flocculates, 4 mL of co-surfactant (1-butanol) are also added. The optimised protocol involves alternating the additions of water and the co-surfactant. Finally, 5.4 mL of precipitating agent, ammonia solution, are slowly dripped. The mixture is stirred for 1.5h at room temperature. The solid phase is then collected by centrifugation, washed twice with ethanol and dried under a hood for 2 days. The dried powder has been manually ground before being calcinated at 120 °C for 6 h. The amounts of cerium and iron were calculated to obtain a nominal composition expressed as a molar % of iron equal to 0 mol % (CeO₂), 0.5 mol % (Fe0.5), 2.5 mol % (Fe2.5), 5 mol% (Fe5) and 10 mol % (Fe10). Samples Fe2.5 after its use as a catalyst for the ibuprofen degradation under visible light was labelled Fe2.5_post reaction.

178 2.2 Structural, morphological and surface characterization

179 Thermogravimetric analysis was performed on Mettler-Toledo TGA/SDTA 851e instrument. The
180 curves were recorded in air increasing the temperature from 25 to 800 °C at the rate of 10 °C/min.

181 Inductively coupled plasma mass spectrometry (ICP-MS) analysis (ICAPQ Thermo Scientific) was
182 applied to determine the effective composition of the prepared catalysts, expressed as Fe/Ce molar
183 ratio. Before analysis, samples are subjected to an extraction process with a hot nitric acid solution to
184 ensure complete dissolution of the interest elements. The subsequent dilutions method is used to
185 achieve the concentration range used for calibration curve preparation.

186 X-ray powder diffraction (XRPD) was performed on a Philips X'Pert diffractometer equipped with a
187 Cu K α radiation (2θ range = 5° - 90°; step = 0.02° 2θ ; time per step = 1 s). Lattice parameters and
188 cell volumes were determined by UnitCell Software, while the crystallite size (L) has been calculated
189 by Scherrer formula: $L = \frac{k\lambda}{\beta \cos\theta}$, k is a constant equal to 0.90, λ is the X-ray wavelength equal to
190 0.154 nm, β is the full width at half maximum, and θ is the half diffraction angle.

191 The optical properties of the powders were recorded on a UV-Vis Varian Cary 5000
192 spectrophotometer equipped with a DR integration sphere in the 200–600 nm range. The indirect
193 band gap values are obtained by applying the Tauc plot method referring to the formula
194 $(F(R)h\nu)^{1/2} = f(h\nu)$.

195 The vibrational properties of the samples have been analysed with Raman spectroscopy. Spectra were
196 collected and recorded at room temperature with a LabRAM HR spectrometer (Jobin Yvon-Horiba),
197 using a X50 confocal microscope and an excitation wavelength of 532 nm. The excitation power was
198 kept low to ensure no photodegradation of the samples. The spectra were dispersed with 1800 gr/mm
199 grating, leading to a 1 cm⁻¹ accuracy.

200 Transmission Electron Microscopy characterization was carried out with a Thalos F200X instrument
201 (ThermoFisher) and Energy Dispersive X-ray spectroscopy (EDX) spectra were acquired with four
202 Silicon drift detectors (SDD). The catalysts as dry powders were dispersed in isopropyl alcohol and
203 subsequently drop-casted onto Cu holey carbon grids. Before insertion in the TEM column, the
204 samples were plasma-cleaned in Ar atmosphere. Thermo Scientific Velox software was used for the
205 analysis of TEM and EDX data. The crystallographic model for cubic CeO₂ (Fm-3m space group) is
206 provided in the Crystallography Open Database (COD ID: 4343161). To complete the morphological
207 characterization a field emission scanning electron microscopy (FE-SEM) was used (ZEISS
208 MERLIN instrument (Oberkochen, Germany)).

209 Textural properties have been evaluated through N₂ physisorption and desorption at 77K
210 (Quantachrome Autosorb1 Instruments.). Before the measurement, the sample was outgassed under
211 a high vacuum at 120°C for 3 hours to remove pollutants previously adsorbed. From the isotherm
212 obtained by nitrogen adsorption, the specific surface area (SSA) of the samples was calculated
213 according to the BET (Brunauer–Emmet–Teller), total pore volume, V_p, was determined from the
214 amount of adsorbed N₂ at p/p°=0.98. BJH pore size distribution was determined by the desorption
215 branch of isotherms [48,49].

216 X-ray photoelectron spectroscopy (XPS) measurements were carried out in a Prevac spectrometer
217 using a focused monochromatic Al K α X-ray source (1486.6 eV) with a pass energy of 40 meV for
218 survey scans and 20 meV for detailed scans. Despite our efforts, sample charging occurred and was
219 only partially compensated by an electron flood source. Binding energies were then shifted from one
220 core level to another. To analyse the spectra, the O1s signal was shifted to reach O α at 529 eV, while

the Ce3d signal referred to as v''' was set at 898.4 eV. Some peak broadening may have resulted from the residual charge. All the peaks were fitted with a Voigt shape function.

ζ -potential curves were obtained by measuring the electrophoretic mobility as a function of pH at 30°C with a Litesizer (Anton Paar Instruments, Worcestershire, UK). The samples were prepared with a starting concentration of 1 mg/50mL, and subsequently, 0.1 M NaOH or 0.1 M HCl were added to varying the pH. The ζ -potential measurements were carried out in an Omega cuvette (Anton Paar) accessory. The measurements were performed in triplicate.

FT-IR 4700LE (JASCO, Tokyo, Japan) using the ATR (attenuated total reflectance) was used to obtain Fourier transform infrared (FTIR) spectra, the spectrum was obtained at a resolution of 2 cm^{-1} over the range of 400-4000 cm^{-1} . Firstly, the sample of pristine photocatalyst Fe2.5 was mixed with potassium anhydrous bromide (KBr) (m/m, 1:2000), and the mixture was pressed to obtain a pellet. KBr was used also as reference material. To identify the interaction between IBU and Fe2.5 catalyst, the pellet of Fe2.5 was covered with a drop of saturated IBU solution and dried in an oven at 60°C for one hour before the analysis.

2.3 Computational Details

Density Functional Theory (DFT) calculations were performed within Periodic Boundary Conditions (PBC) using the Perdew-Burke-Ernzerhof (PBE) exchange-correlation functional based on the generalized gradient approximation (GGA) [50] and ultrasoft pseudopotentials [51]. The spin polarized Kohn-Sham equations were solved in the planewave pseudopotential framework, with the wavefunction basis set and the Fourier representation of the charge density being limited by kinetic cutoffs of 60 and 500 Ry, respectively. The Quantum Espresso code [52] was employed for all calculations. It is well established that a reliable description of both stoichiometric and reduced ceria-based materials can be achieved by adding a Hubbard U term to the GGA energy functional acting on the f states of the Ce ions. Therefore, all the calculations reported in this work were performed at the DFT+U level, as implemented by Cococcioni and de Gironcoli [53], employing a U value of 4.5 eV. This is consistent with previous literature reporting values between 4.5 and 5 eV [54–65]. In all calculations the Brillouin zone integration was performed on the Γ point only.

All the calculations were performed on the (111) termination of CeO₂ (Fig. SI.1), being the most stable one and the most present in the experiment (see Fig. 1a). We are aware that this represent a simplification of the system prepared from experiments but from a computational point of view is not possible to capture the complexity of the real system. The Ibuprofen (IBU) molecule is anionic in experimental pH-neutral conditions [66], therefore it was simulated in its deprotonated form when adsorbed on the CeO₂(111) surface. The proton released by the molecule is transferred to O3c (tri-coordinated O) atoms of the surface similarly to previous theoretical studies [67–70].

The CeO₂ (111) surface was modelled using a (5x4) slab supercell with three O-Ce-O trilayers (180 atoms) and separated by more than 20 Å of vacuum in the direction perpendicular to the surface. During the optimizations, the bottom tri-layer of the slab was fixed to simulate the equilibrium bulk-like position, while the upper two tri-layers and the organic ligand were fully relaxed. The O-defective systems were modeled by removing O3c and O4c atoms from the surface and subsurface layers of the CeO₂ (111) slab (VO_x). The formation energies of the oxygen vacancies were computed as $E_{\text{FORM}(\text{VO}_x)} = E_{\text{VO}_x} - E_{\text{CeO}_2} + \frac{1}{2}E_{\text{O}_2}$, where E_{CeO_2} is the energy of the stoichiometric surface, while E_{VO_x} and E_{O_2} are the energies of the surface with oxygen vacancies and of the gas phase O₂ molecule, respectively.

The adsorption energy of IBU was computed using the formula $E_{ads} = E_{CeO_2/IBU} - (E_{CeO_2} + E_{H-IBU})$, where $E_{CeO_2/IBU}$ is the energy of the combined system (namely the surface plus the anionic IBU), E_{CeO_2} is the energy of the stoichiometric and/or O-defective surface (E_{VOx}) alone, and E_{H-IBU} is the energy of the neutral IBU in gas phase.

The substitutional and interstitial Fe-doping effects were evaluated by replacing and adding Ce atoms in all considered systems.

In order to analyze the thermodynamic stability of different structures in the absence and in the presence of i) Fe dopant and ii) oxygen vacancies as a function of temperature and pressure, the formalism of approximate *ab initio* thermodynamics was employed [71–74]. According to this formalism, the Gibbs energies of the formation of the different ceria systems depend on the temperature and pressure through the following expression (Eq.1):

$$\Delta G_{ads}(T, p) = \frac{1}{A} \{ E_{tot} - E_{CeO_2} + N_O^V \mu_O(T, p) + N_{Ce}^V [E_{CeO_2}^{bulk} - 2\mu_O(T, p)] - \mu_{Fe} \} \quad (1)$$

where A is the surface area, E_{tot} and E_{CeO_2} are the total energies of the considered ceria system and stoichiometric ceria surface, respectively. The quantities N_O and N_{Ce} represent the number of O and Ce vacancies present in the structure under consideration, whereas $E_{CeO_2}^{bulk}$ is the energy of a formula unit of the CeO_2 bulk phase. Finally, μ_{Fe} and μ_O are the oxygen and iron chemical potentials. The chemical potential of Fe, μ_{Fe} , is set to be the total energy per atom of the bulk Fe crystal, whereas the upper bound of the chemical potential of O_2 , $\mu_O(T, p)$, is given by the total energy of molecular oxygen, $\frac{1}{2} E_{O_2}$. This upper bound is taken as the zero of our energy scale by using $\Delta\mu_O(T, p) = \mu_O - \frac{1}{2} E_{O_2}$. In addition, assuming that volume and entropy contributions are negligible in $\Delta G_{ads}(T, p)$ [73], the Gibbs energies are approximated by the total energies of our DFT calculations.

Electronic properties were investigated only for the most stable systems. In addition, to determine the approximate oxidation states of anions and cations the charge analysis was performed following the Bader's theory since the charge enclosed within the Bader volume can be considered a good approximation of the total electronic charge of an atom [75–77].

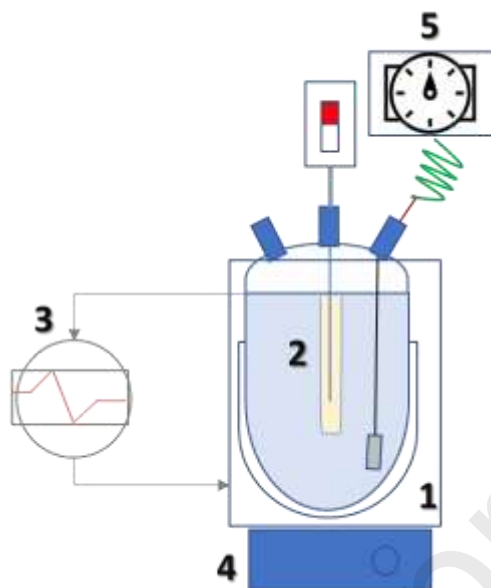
290

2.4 Catalytic and kinetic tests

The photodegradation experiments were conducted in a 1.5 L jacketed glass vessel, closed with a three-neck lid, as reported in Scheme 1. The reactions were carried out using a co-axial lamp, connected to the reactor through the central neck of the lid. In particular, two different lamps were used: a lamp irradiating in the visible region (Sylvania T5, with a power of 4W and a colour temperature of 6500 K, solar emission spectrum, potential difference 220V, and geometry 14 cm x 1.5 cm), or a lamp irradiating in the UV region (Toshiba FL4BLB, with a power of 4W and emission at a wavelength of 365 nm, potential difference 220 V, and geometry 15 cm x 1.5 cm). The irradiance

of the lamp in the experimental apparatus was estimated to be 510 W/m². One neck of the lid was left free for collecting samples during the reaction, while the last neck is used for measuring the solution temperature through a dedicated thermocouple. The reaction temperature was controlled using an ultra-thermostat while the dispersion agitation was ensured by magnetic stirring. The airflow rate was set through an electronic gas flowmeter regulator (supplied by Bronkhorst). Air dispersion was enhanced by connecting the outlet of the gas flowmeter regulator to a sintered filter of 50 mesh,

immersed in the liquid-solid dispersion. This technical solution allowed it to reach a high gas-liquid surface area, minimizing eventual gas-liquid mass transfer limitations.



307
308

Scheme 1: Reaction system sketch. 1 Batch reactor, 2 lamps, 3 ultra-thermostat, 4 stirring plates, 5 digital flowmeter regulator.

311

As ibuprofen is characterized by relatively low solubility in water (21 mg/L, 25 °C) [78], the solutions (with an initial concentration, $C_{IBU,0}$, of 12.4 mg/L) have been prepared and kept in stirring overnight at room temperature and covered with aluminum foil to protect the solution from the light. After the total dissolution of ibuprofen, the solution is transferred into the reactor, stirred at 750 rpm and warmed up at 30°C. At this point, the catalyst ($\rho_B=0.07\text{g/L}$) was loaded into the reactor. It is important to underline that the operation conditions were chosen from preliminary tests to measure the catalytic activity of the catalysts synthesized in this work.

Three different types of kinetic experiments were conducted: (i) adsorption; (ii) under UV irradiation; (iii) under visible irradiation. In the first case, the system was covered with aluminum foils to prevent any contact with the solution with the solar light. In the other two cases, a specific lamp was adopted as previously stated. Also in the latter cases, the system was covered with aluminum foil. Airflow was adjusted using the digital flow meter and was set at a fixed flow (50mL/min), allowing it to reach full saturation of oxygen in the water. Of course, no air was fed during the adsorption experiments. The reaction was then started by switching on the lamp and prosecuting until a maximum time of 5h.

Before any subsequent operation, a first sample was collected to check the initial ibuprofen concentration ($C_{IBU,0}$); subsequently, samples were collected every 30 minutes for the first 2 hours of reaction, and every hour for the remaining three hours (0, 30, 60, 90, 120, 180, 240 and 300 minutes). Each sample was then centrifuged at 3300 rpm for 30 minutes, and the resulting liquid sample was analyzed by UV-VIS spectroscopy (UV-Vis Jasco V-550), see Supplementary Information for details (Fig. SI.2 and Equation SI-1, i.e., the calibration curve).

332

2.4.1 Regeneration experiments

The stability of the most active catalyst was tested via reuse experiments, adopting the following reaction conditions: $T=30^{\circ}\text{C}$, $C_{\text{IBU},0}=12.4\text{mg/L}$, $\rho_{\text{B}}=0.07\text{ g/L}$, visible light, Fe2.5 catalyst. In particular, the catalyst was recovered after each photodegradation test, by filtering it on a Buchner funnel. Before reusing it, the catalyst was washed several times on the funnel itself using water, and then was recovered by filtration and oven-dried for 12 h at 60°C . The procedure was repeated for four cycles [79].

2.4.2 Photodegradation products identification

A dedicated kinetic experiment was performed to identify the reaction products. The experiment was performed using the Fe2.5 catalyst under visible irradiation, adopting an initial concentration of ibuprofen of 12.4 mg/L , a catalyst loading of 0.07 g/L , a stirring rate of 750 rpm , and a temperature of 30°C .

LC-MS analysis was performed by an Agilent HPLC system (1260 Series) coupled to an Agilent 6230 TOF mass spectrometer apparatus. The HPLC separation was carried out on a reverse-phase C18 column (Poroshell 120 EC-C18 $3\times 50\text{ mm}$ $2.7\text{ }\mu\text{m}$ from Agilent Life Sciences) by using water and acetonitrile as mobile phases A and B, respectively, both acidified with 0.1% formic acid. A linear gradient was employed by increasing mobile phase B from 50% to 95% over 9 min at a flow rate of 0.3 mL min^{-1} . The injection volume of each sample was $20\text{ }\mu\text{L}$ and the MS source was an electrospray ionization (ESI) interface in the positive ion mode with a capillary voltage of 3000 V , gas temperature at 325°C , dry gas (N_2) flow at 5 L min^{-1} and the nebulizer pressure at 35 psi , the fragment at 50 V . The MS spectra were acquired in a mass range of $50\text{--}1000\text{ m/z}$ with a rate of 1 spectrum/s, abundance threshold 200 (0.015 relative thresholds).

GC-MS analyses were performed on a 5390 MSD quadrupole mass spectrometer (Agilent Technologies) equipped with a gas chromatograph by using a Polysiloxane DB-5 column ((5%-Phenyl)-methylpolysiloxane, Agilent Technologies) ($30\text{ m}\times 0.25\text{ mm}\times 0.25\text{ }\mu\text{m}$) from Phenomenex. The injection temperature was 250°C , the oven temperature was increased and held at 50°C for three minutes and then increased to 150°C at 10°C/min , increasing to 230°C at 14°C/min and finally to 280°C at 15°C/min held for 7 min. Electron Ionization mass spectra were recorded by continuous quadrupole scanning at 70 eV ionization energy, in the mass range of m/z $40\text{--}550$ analysis. Each sample was measured in triplicate.

3. Results and discussion

3.1 About the adopted reverse micelle approach

Although the co-precipitation-based synthesis method is extensively used, with a very simple set-up, it suffers from poor control over particle size and homogeneity in mixed oxide systems [80].

In this work, the aforementioned drawbacks were overcome by channelling the reactions that normally take place in aqueous media into the small domains of reverse micelles. Specifically, an aqueous solution containing the iron and cerium precursor was added to a solution of the non-ionic

surfactant, Brij C10, in cyclohexane, generating a water-oil microemulsion. The cage-like environment provided by the microemulsion with the simultaneous presence of the cerium and iron precursors, enabled excellent control of the final stoichiometry, resulting in homogeneity and mixing on an atomic scale, ultimately favouring the effective inclusion of iron heteroatoms in large amounts, as discussed hereafter [80–84].

The synthesis parameters, in particular the type and nature of the surfactant and the water/surfactant ratio, were optimized after careful variation. The value w , defined as the water-surfactant molar ratio ($[\text{H}_2\text{O}/\text{BrijC10}]$), is considered a key parameter for tuning the size of the spherical droplet, affecting the dynamics of water and defining the spatial confinement of the reaction [85,86]. The occurrence of chemical reactions was clearly visible through the colour change of the macrosystem, which moved from a colourless/pale yellow to purple-dense, turning yellow after the fixed reaction time (estimated at one and a half hours). The formation of the purple slurry was attributed to the generation of insoluble Ce^{3+} species that after the complete oxidation turned to yellow Ce^{4+} species [46,87]. The obtained material was recovered by centrifugation, washed to purify from the oil/surfactant, and left catalysts to dry under the hood. Then, the dried powders were heat treated at 120 °C for 6h. The absence of significant quantities of organic residues, confirming the effectiveness of the protocol without the need to use high calcination temperatures, was revealed by the thermogravimetric analysis (Fig. SI.3). The thermal behaviour of the material was explained by identifying three regions in the thermogravimetric curve: (i) from room temperature to 120 °C where the weight loss is due to physisorbed water, (ii) 200-350 °C related to the removal of chemisorbed water occurs, (iii) 400-800 °C characteristic of combustion of organic compounds [88–90]. The synthesis procedure was designed to ensure the highest reproducibility. The effective presence of iron species into the ceria phase was highlighted by the different colour of the powders, changing from light yellow for pure ceria to a reddish-yellow with increasing in the Fe contents (Fig. SI.4).

The results of the quantitative analysis performed by ICP-MS are shown in Table 2. The Fe/Ce ratio is in excellent agreement with the nominal value, showing that the adopted synthesis protocol effectively preserves stoichiometry and avoids material losses during the production steps.

3.2 Structural, textural and surface properties

Cerium oxide occurs in the fluorite phase where the cerium atoms are organised in a face-centered cubic lattice structure with 8-fold coordination, while the oxygens are present as OCe_4 units [91]. Defect chemistry and the numerous studies conducted on doped and undoped nanometric CeO_2 crystal structure have unequivocally stated that its reactivity and performance of heterogeneous catalysis are surprisingly modulable by engineering the defects and surface structure using a flexible and reliable synthesis procedure [92,93].

XRD diffraction patterns of ceria and Fe-containing ceria samples are reported in Fig. 1a. The pristine ceria shows an XRD profile corresponding to a cubic fluorite structure (JCPDS files 34-0394), where the peak at 28.5°, 33.3°, 47.1° and 56.1° can be associated with the planes 111, 200, 220, and 311, respectively [46]. Although the diffraction patterns of Fe-containing samples reveal that the F-type crystalline structure is retained, the diffraction lines show a progressive shift towards higher 2-teta values, Fig. 1b [46]. As reported by many authors, an isomorphic substitution of Ce^{4+} ions (ionic radius 0.97 Å, coordination number CN=8) by smaller Fe^{3+} ions (ionic radius 0.78 Å, CN=8) can account for the lattice shrinkage, appearing as a displacement of the diffraction patterns towards higher angles [25,93]. The observed lattice constraint follows Vegard's law [94] as suggested by the lattice parameters reported in Table 2 and further evidenced by Fig. SI.5. Substitutional doping with the formation of oxygen vacancies, one oxygen vacancy paired with two M^{3+} for charge

neutrality, is a dominant mechanism for ceria doped with aliovalent cations [93,95]. Nevertheless, the small size of Fe^{3+} also allows for a dopant interstitial compensation mechanism where three Fe^{3+} in substitution sites are coupled to one in interstitial sites. This last mechanism leads to a decrease in oxygen vacancy concentration. The further increase in iron content may subsequently promote epitaxial growth on the CeO_2 surface [25,96]. In this scenario, the adopted synthesis method was decisive in promoting substitutional doping, limiting the formation of crystalline phases attributable to iron oxides. The type of doping was also supported by DFT calculation (*vide infra*).

Moreover, the control exerted by the aqueous core during synthesis is successfully reflected in the formation of small-sized crystallites (Table 2), compared to the more conventional methods [96–98]

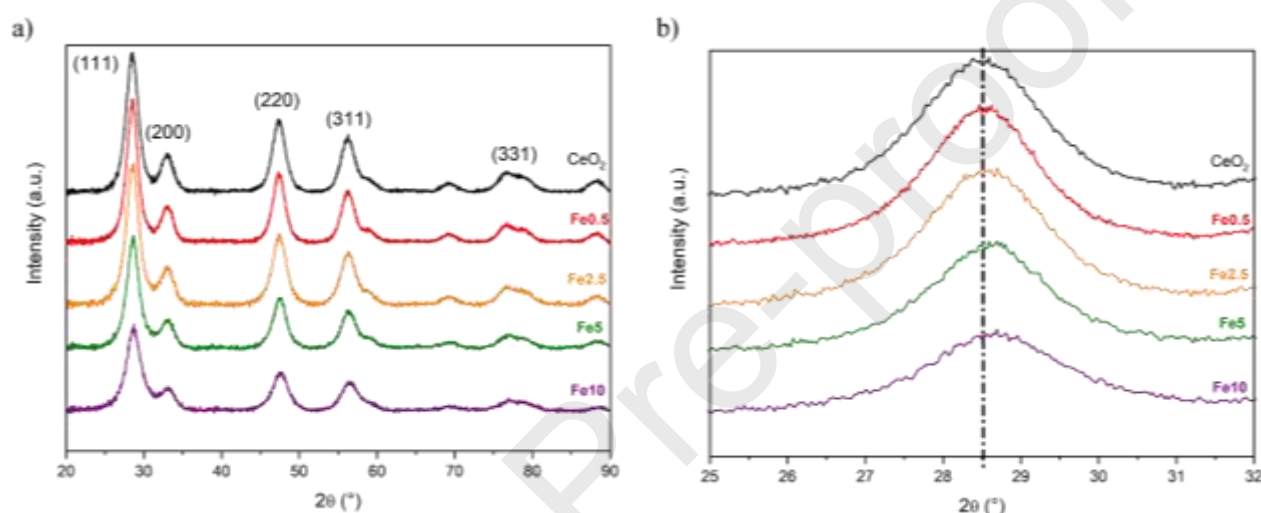


Fig. 1: a) XRD patterns of the synthesized samples in 2θ range 20°–90° and b) enlarged view of (111) diffraction peak.

Table 2: Summary of analytical data: chemical composition calculated from ICP-MS elemental analysis and structural parameters obtained from the cell refinement of the XRD patterns.

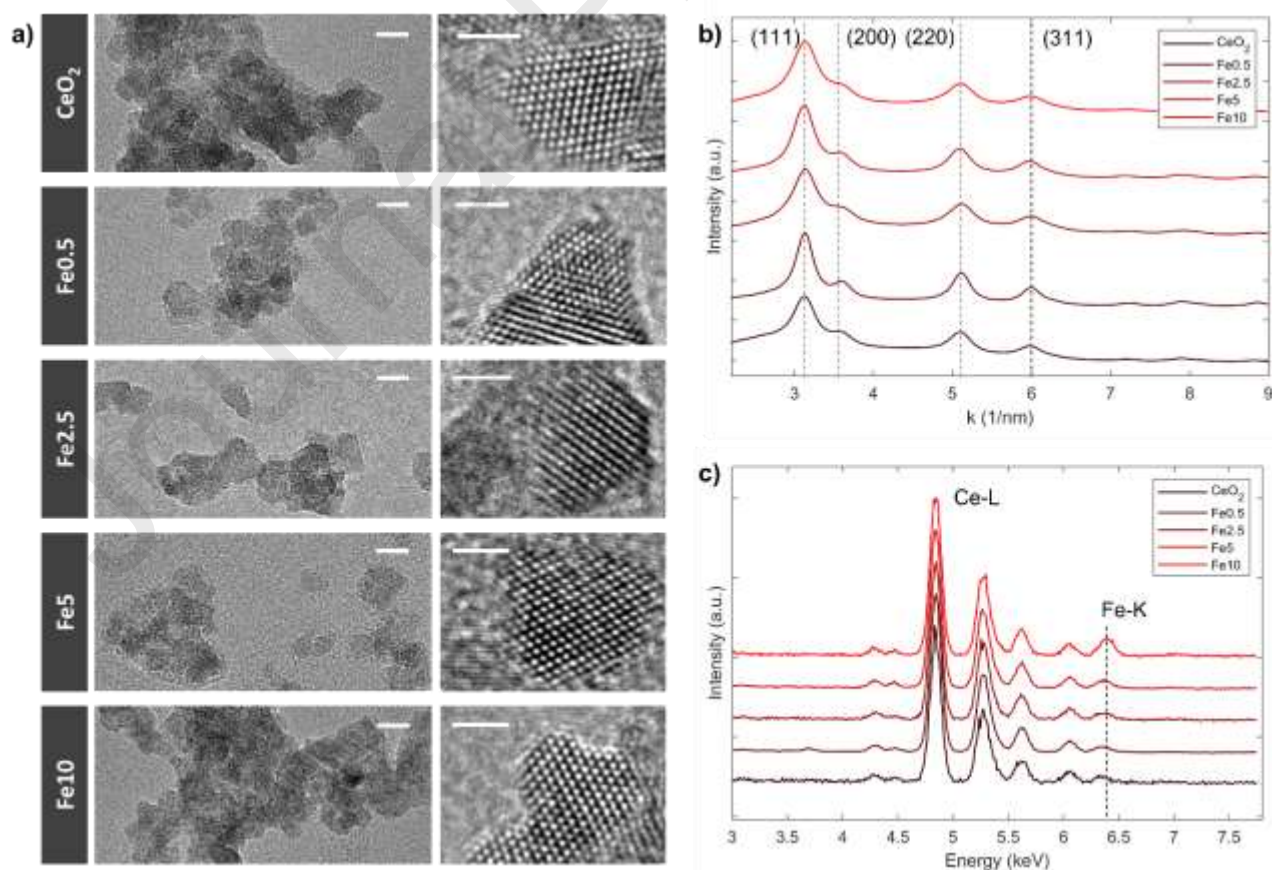
Sample	Nominal ratio		Actual ratio		
	Fe/Ce (molar %)	Fe/Ce ICP-MS (molar %)	Lattice Parameter (Å) ^a	Cell Volume (Å ³)	Crystallite size, L (Å) ^b
CeO_2	-	-	$5.4269 \pm 3 \cdot 10^{-4}$	$159.83 \pm 2 \cdot 10^{-2}$	42

Fe0.5	0.5	0.66	$5.4259 \pm 3 \times 10^{-4}$	$159.74 \pm 2 \times 10^{-2}$	44
Fe2.5	2.58	2.87	$5.4234 \pm 3 \times 10^{-4}$	$159.52 \pm 2 \times 10^{-2}$	40
Fe5	5.31	4.3	$5.4162 \pm 3 \times 10^{-4}$	$158.89 \pm 2 \times 10^{-2}$	40
Fe10	11.2	11.1	$5.4030 \pm 3 \times 10^{-4}$	$157.72 \pm 2 \times 10^{-2}$	34

437 ^a for fluorite phase; ^b Calculated using Scherrer equation due to (1 1 1) plane

438

439 Further insight into the morphology and structure of the iron-doped ceria catalysts is provided by
 440 Transmission and Scanning Electron Microscopy (Fig. 2 and Fig.SI.6, respectively). Based on TEM
 441 images (Fig. 2a), the catalyst powders are constituted of aggregates of approximately spherical
 442 nanoparticles. Inspection of high-resolution images reveals that the nanoparticles are single
 443 crystalline, with a crystalline structure corresponding to cubic CeO₂ (Fm-3m space group). It is worth
 444 pointing out that the characteristic size of the nanoparticles is in the order of 5 nm or lower, in
 445 accordance with the crystallite size estimation based on the application of the Scherrer formula on
 446 XRD data.



447

Fig. 2: a) TEM high-resolution images of the different Fe-doped CeO₂ catalysts (scalebar: left column 5 nm, right column 2 nm). Rotationally-averaged selected-area electron diffraction patterns are provided in b). Representative EDX spectra are shown in c).

Moreover, from high-resolution images, there is no evidence of secondary iron-containing crystalline phases. This is confirmed by rotationally-averaged selected area electron diffraction (SAED) patterns, such as the ones provided in Fig. 2b. For each Fe-containing catalyst sample, the diffraction patterns only show peaks corresponding to the (111), (200), (220), and (311) family of crystallographic planes of cubic CeO₂, in agreement with the previously discussed XRD results. Finally, EDX spectra of the catalysts (Fig. 2c) indicate the presence of Fe in all the samples besides pristine CeO₂. It is interesting to notice that the contribution from the Fe K α line (~ 6.4 keV) in EDX spectra correlates with the nominal increase of Fe in the catalysts, confirming that the crystalline nanoparticles host an increasing amount of Fe ions, without significant changes in the F-type crystalline structure of CeO₂. The SEM micrographs (Fig.SI.6) show a quasi-spherical shape of nanoparticles with a uniform distribution, in agreement with the morphologies obtained from TEM data. To further confirm the presence of Fe in all samples a compositional analysis has been done also by EDS. The atomic ratio Fe/Ce obtained (average in 5 spots) is in good accordance with the theoretical molar ratio and experimental ICP data (see Table SI.1 for details). The optical properties of the prepared materials were evaluated by UV-Vis diffuse reflectance spectroscopy. The D(R) spectra are shown in Fig. 3a. The UV-Vis spectrum of pure CeO₂, black line, consisted of a strong absorption band located in the 200-400 nm range where different transitions can be observed. The absorption at low wavelength, one centered at 215 nm and the other at around 275 nm (blue rectangle and green rectangle in Fig. 3a, respectively), are generally attributed to charge-transfer transitions between O 2p and Ce 4f orbital. In particular, the absorption due to Ce³⁺ \leftarrow O²⁻ charge transfer is observed at 215 nm while the peak at a higher wavelength is ascribed to Ce⁴⁺ \leftarrow O²⁻ transition [97,99]. The shoulder at 340 nm is assigned to interband transitions [46]. The reported behaviour is also observed in the spectra of iron-containing samples; however, a careful examination reveals some modifications.

The shift to the lower wave number of the main peak recorded for the Fe_{0.5} sample could be caused by the isolated Fe³⁺ species[100,101]. Indeed, Fe Oh and Td species show the typical transitions in the UV range, allowing a not easy assignment due to overlapping absorption range with ceria. The absorption at 215 nm appears more prominent when increasing the iron doping percentage up to Fe_{2.5}, thus suggesting a more pronounced presence of defective sites [102]. The spectrum recorded for the Fe₁₀ sample (purple curve) shows a feature at about 380 nm that is generally assigned to the presence of oligomeric hematite-like clusters, as reported by Schwidder et al [42]. However, the typical d-d transitions of α -Fe₂O₃, located at 533 nm, are not observed. The lack of stoichiometric iron phase is in accordance with the XRD results, whereas the oligomeric clusters are in accordance with the Raman results, which evidence a contribution at (~ 670 cm⁻¹) only into the sample at higher iron loading (*vide infra*). The spectra of all the iron-doped catalysts show a red shift in the absorption edge, indicative of the Ce-Fe interaction.

The effect of iron doping on the optical band gap was assessed by Tauc plot relation. In Fig. 3b (F(R)(h ν)^{1/2}) is plotted versus the photon energy, h ν , and the indirect band gap energy (E_g) was obtained by applying the double tan approximation [103]. The band gap value of pristine CeO₂ was found to be 3.0 eV. The effective inclusion of the Fe species in the ceria lattice results in a decrease in E_g, ascribable to the introduction of vacant 3d orbitals between the valence and conduction bands of CeO₂ [104].

Table 3 shows that E_g values decrease monotonically with iron content [36,60]. This trend is also observed in the theoretical E_g values calculated for the undoped and Fe-doped CeO_2 discussed in the following DFT study section. The band gap values obtained in the iron-doped samples reported here are somewhat lower than those reported in the literature for the same compositions [36,60,105–107]. Once again, all the previous features can be attributed to the adopted reverse micelle strategies.

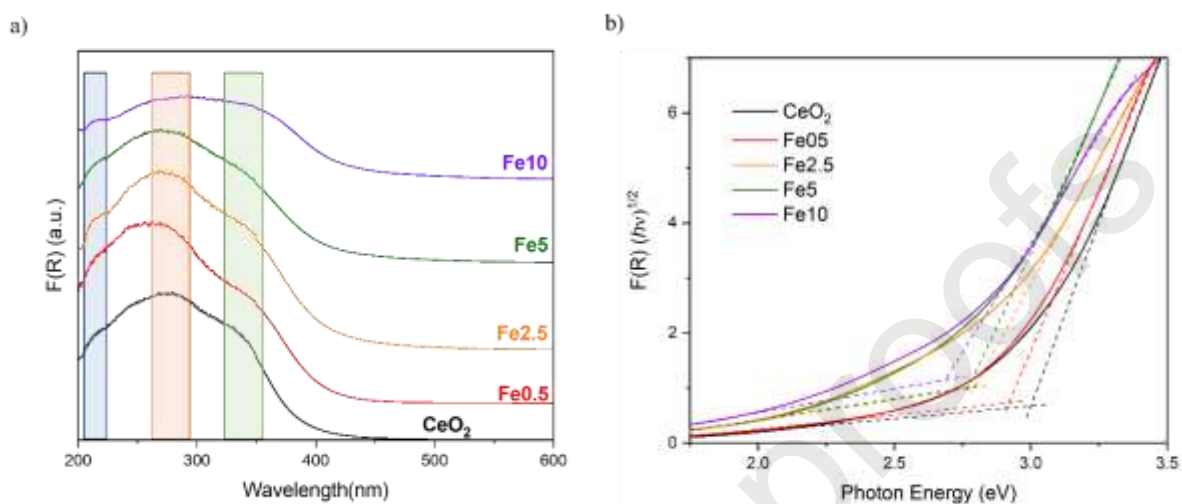


Fig. 3: a) DR UV-Vis spectra of synthesized samples plotted as Kubelka-Munk function $F(R)$. b) The indirect band gap calculation of pristine and Fe-doped porous CeO_2 based on the Kubelka-Munk function by Tauc plot relation using the double tan approximation. CeO_2 (black curve); Fe0.5 (red curve), Fe2.5 (orange curve), Fe5 (green curve) and Fe10 (purple curve).

Significant information on the fate of iron in ceria nanocrystals can be obtained from Raman. The spectra corresponding to the iron-doped samples are shown in Fig. 4a along with that of pure CeO_2 nanocrystals. Three main contributions are observed. The prominent peak corresponds to the F_{2g} peak and it results from the vibration of the O sublattice. It stands at 458.5 cm^{-1} for the pure CeO_2 nanocrystals, some 6.5 cm^{-1} lower than the position of pristine bulk CeO_2 . This shift is consistent with the reported decrease of peak position with particle size reduction [91] and a Gruneisen parameter value of 1.57. For instance, Spanier et al. [108] reported a 4 cm^{-1} redshift for 6 nm nanocrystals. The peak shows an asymmetry towards low wavenumbers. Such an asymmetry is often seen in nanocrystal samples and related to size dispersion [91,109,110].

As iron is incorporated into the nanocrystals, the F_{2g} peak mode is further softened and broadened. Such behaviour was previously observed by Popovic et al. [111] for Fe-doped CeO_2 nanocrystals. The trend is not strictly monotonous with the nominal Fe concentration. Fig. 4b shows the correlation between the F_{2g} peak shift ($\Delta\omega$) and the corresponding variation of the peak FWHM (full-width-at-half-maximum). The variation is linear as previously observed by Popovic et al. However, the slope of our curve is -6.9, slightly higher than that reported in [111], with a value of -5.3. This behaviour originates from two causes: grain size and strain effect (causing homogeneous line broadening) and charges delocalization in oxygen-deficient ceria. Since all the samples have about the same nanocrystal mean size, neither the mode softening nor the line broadening can be attributed to any size effect. The observed linear variation thus results from changes in strain within the nanocrystals and charge delocalization. The two phenomena are hard to disentangle without further modelling.

However, the actual occurrence of such a variation is the signature that the samples are oxygen deficient and that charge delocalization happens for 4f electrons located at Ce(Fe)-VO-Ce(Fe) orbitals. This charge delocalization is generally favourable to the photocatalytic activity. This is confirmed in our case where the sample Fe2.5 shows both the highest delocalization and the highest photocatalytic activity (see Fig. 11). We exclude from our analysis the Fe10 sample that cannot be considered as simply doped ceria since it probably contains oligomeric species at its surface, detrimental to its catalytic activity.

Two supplementary peaks are noticed at 270 cm^{-1} and 606 cm^{-1} respectively. They are assigned to the F_{1TO} and F_{1LO} phonon modes. These vibrations are forbidden in pristine CeO_2 but are often seen in nanocrystal samples as a result of the long-range symmetry breaking of the crystals. The magnitude of the F_{1LO} peak increases with Fe content as evidenced in Fig. SI.7 where the change in the ratio between the F_{1LO} contribution and the F_{2g} contribution is plotted versus the sample composition. The F_{1LO} feature can be assigned to defects involving dopant cation complexes close to VO [112]. It can be clearly observed that moving from sample Fe0.5 to sample Fe2.5 the ratio is almost doubled, indicating the increased presence of the aforementioned VO-related complexes.

For the Fe10 sample, on top of the F_{1LO} feature, a second contribution at approximately 670 cm^{-1} appears. This contribution cannot be assigned to the presence of VO but rather to the presence of Fe at high content [112]. As already mentioned, this sample cannot be considered in the strict sense as doped ceria.

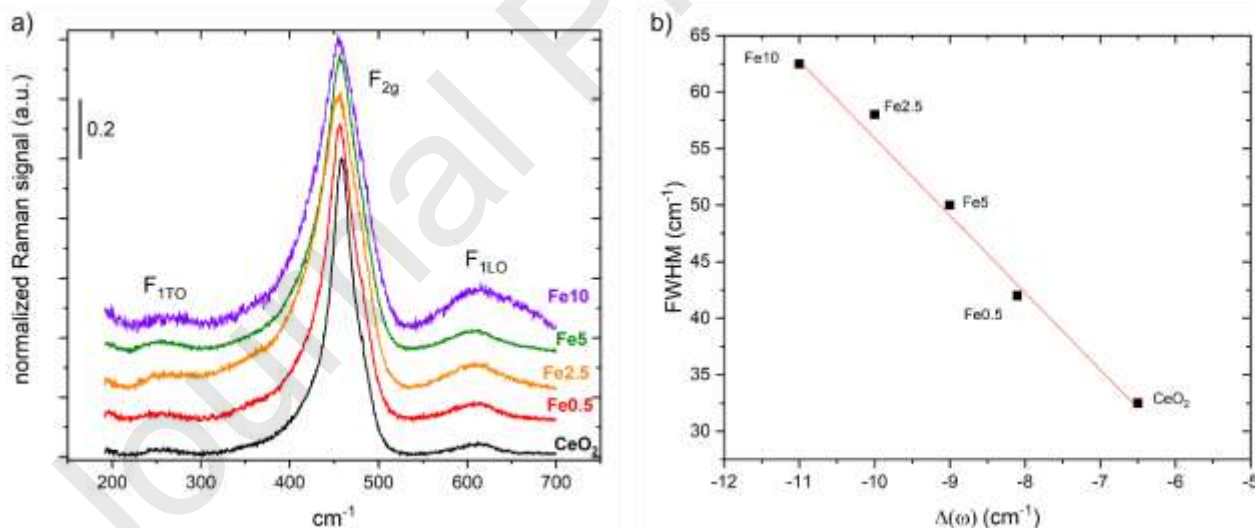


Fig. 4: a) Raman spectra of pristine and Fe-doped CeO_2 nanocrystals for different doping concentrations. All spectra are normalized to the maximum intensity of the F_{2g} peak. b) Variation of the F_{2g} peak FWHM concerning its position variation as a function of the Fe concentration in CeO_2 nanocrystals. $\Delta\omega$ is referred to the value of pristine CeO_2 .

The textural properties were evaluated by N_2 adsorption at low temperatures ($-196\text{ }^\circ\text{C}$). The adsorption/desorption isotherms, Fig. SI.8a, resemble type IV, typical of mesoporous material with a hysteresis loop indicating block-neck pores shape (hysteresis type H2). All the studied samples have

a BET-specific surface area higher than or equal to $180 \text{ m}^2 \text{ g}^{-1}$ Table 3, with the exception of the sample Fe10 that shows a surface area of $274 \text{ m}^2 \text{ g}^{-1}$. Considering that the surface area is interparticle, the discordant value of Fe10 can be explained by the smaller particle size, Table 2. The limited particle growth observed at high iron contents may be correlated with the presence of iron-containing species on the surface [46,93]. The pore size distribution (PSD) evaluated by the BJH method on desorption branches, Fig.SI.8b, suggests that the synthetic route is effective for the preparation of mesoporous (doped) ceria.

The designed reverse micelles synthesis route allows for obtaining a very high surface area compared, not only with different methods [33,107,113] but also with similar procedures reported in the literature [46,47].

Table 3: Energy of band gap (Eg) and textural properties of pristine and Fe-doped CeO_2 sample

Sample	Eg (eV)	BET SSA ($\text{m}^2 \text{ g}^{-1}$)	Vp ($\text{cm}^3 \text{ g}^{-1}$)
CeO_2	3.00	182	0.196
Fe0.5	2.91	180	0.184
Fe2.5	2.79	191	0.188
Fe5	2.77	189	0.192
Fe10	2.68	274	0.280

In order to have a better surface a XPS analysis was spectrum, although highly deconvoluted with some precautions [114,115]. Here Ce3d XPS spectra, shown in Fig. 5a, were solved with five $3d_{5/2}$ components denoted as v_0 (880.6 eV), v (882.6 eV), v' (885.45 eV), v'' (888.85 eV) and v''' (898.4 eV) with ± 0.3 eV resolution and their $3d_{3/2}$ counterparts (called u_x) separated by 18.45 eV (± 0.15 eV) with a ratio u_x/v_x of 1.5(± 0.1). The amount of surface Ce^{3+} ion was determined using the area of v_0 , u_0 , v' and u' peaks, while v , u , v'' , u'' , v''' and u''' were assigned to surface Ce^{4+} ion.

The two ions appear for different environments of Ce atoms, resulting in different charge transfers. Ce^{3+} is indeed present in Ce_2O_3 , while CeO_2 is made of Ce^{4+} ions. Since the O1s core level is sensitive to changes in the coordination of the oxygen atoms, its deconvolution should also allow the evaluation of the charge transfer between oxygen and cerium atoms. Three components are usually considered to resolve XPS spectra of the O1s core level in CeO_2 . The first one, labeled $\text{O}\alpha$ at 529 eV, is usually associated with lattice oxygen, i.e. Ce^{4+} in CeO_2 . Following [116], $\text{O}\beta$ feature at 531 eV and $\text{O}\gamma$ feature at 532 eV are attributed to surface hydroxyl groups, resulting from the dissociation of adsorbed water and irreversibly adsorbed molecular water, respectively. These energies (± 0.1 eV) were fixed to fit our XPS data, as shown in Fig. 5b. Finally, relative atomic concentration was

calculated as the ratio of the normalized intensity of one element with a given valence over the normalized intensity of that element (whatever the valence), with a sensitivity factor calculated as the product of theoretical inelastic mean free path and cross section.

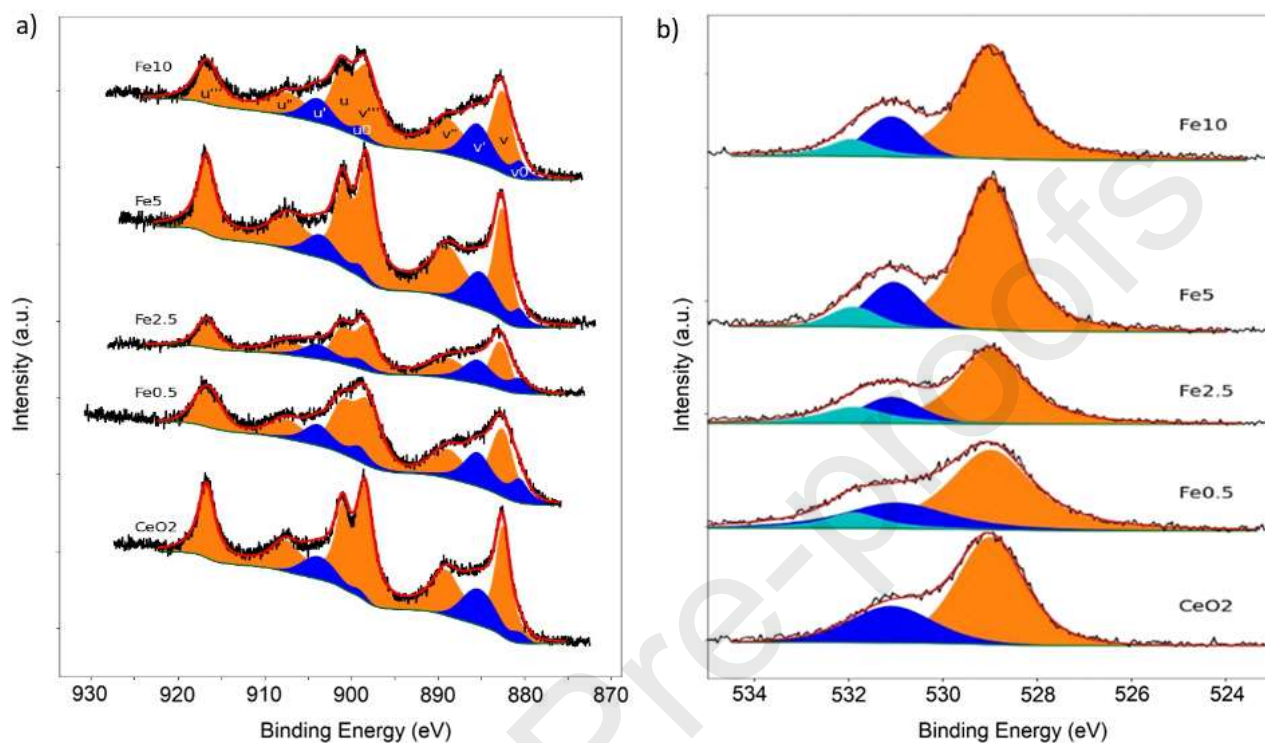


Fig. 5: Experimental and fitted XPS spectra. Ce3d (a) and O1s (b) core level spectra as a function of the Fe concentration in CeO₂ nanocrystals. Experimental data are in black, Shirley background in green. The sum of 5 components of doublets (2 of Ce³⁺, blue area, 3 of Ce⁴⁺, orange area) are used to fit the Ce3d signal (a) or of 3 components (O α , O β and O γ , areas in orange, blue and cyan, respectively) to fit O1s signal in red.

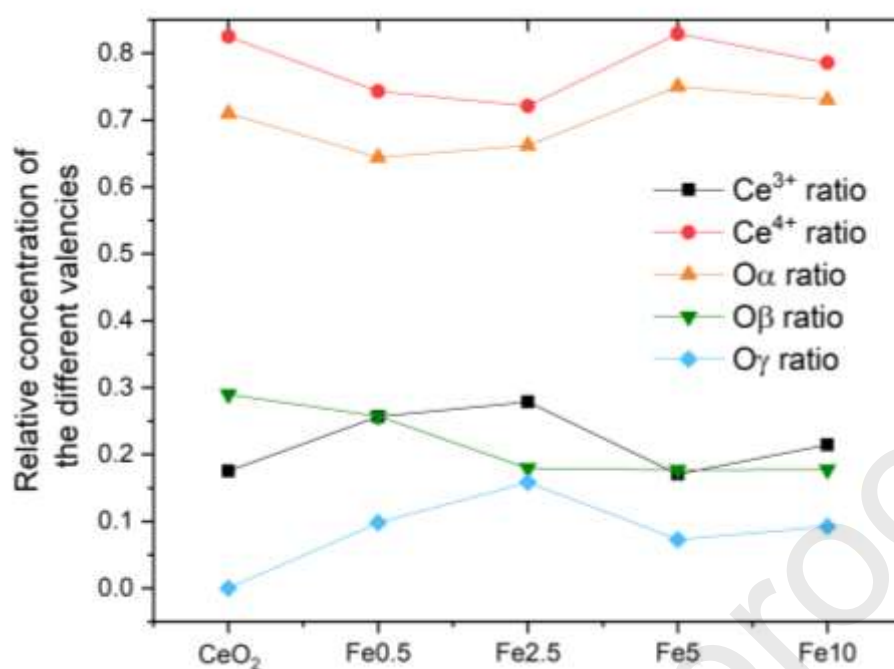


Fig. 6: Relative atomic composition of the synthesized pristine and doped CeO₂ nanocrystals as a function of Fe content.

As shown in Fig. 6, the Ce⁴⁺ relative atomic concentration follows nicely that of O_α. Both signals decrease as the Fe content increases from CeO₂ to Fe2.5 and next decrease and reach an almost constant value. This is consistent since both signals come from the CeO₂ units in the nanocrystal bulk. Remarkably, the variation of the Ce³⁺ relative atomic concentration is opposite to that of Ce⁴⁺. This reveals that the increase in Fe content from CeO₂ to Fe2.5 promotes the enrichment of Ce³⁺ within the Ce. Adding more Fe does not lead to more Ce³⁺ ions. On the contrary, it appears that the further addition of Fe atoms, beyond Fe2.5, is less effective in generating Ce³⁺ ions.

As demonstrated by DFT calculations (see below), the generation of Ce³⁺ ions is related to the generation of VOs. The evolution of the oxygen concentration cannot be directly seen in the XPS spectra since, as stated above, there is no XPS feature directly related to VOs. Consequently, even though the analysis of the Ce³⁺ feature remains delicate since the X rays may induce the reduction of ceria during the observation [117], its evolution remains a relevant indication of the VOs concentration. Interestingly, one can note that the minimum Ce⁴⁺ concentration (thus the maximum of Ce³⁺ and VOs concentrations) is concomitant with the maximum catalytic activity.

To conclude the discussion, the analysis of the Fe2p core level signal would have been highly relevant. However, Fe2p signal is very weak, although increasing with doping, and at the same energies as the signal of Ce M45N45V Auger electrons (see supplementary Fig. SI.9). From its analysis only 3% atomic concentration was found when 10% was expected. As XPS is sensitive to the extreme surface (first few nms), it indicates that Fe might be inhomogeneously distributed in the nanocrystals.

3.3 DFT study

3.3.1. Fe-doped CeO₂ surfaces characterization

Density functional theory (DFT) calculations were performed to investigate the effects of Fe-doping on the structural and electronic properties of CeO₂ (111) surfaces. We have considered the scenario in which iron atoms substitute surface and subsurface Ce sites (Fe@Ce) as well as interstitial doping, where Fe atoms occupy interstitial sites in the crystal structure (Fe_{Int}).

The optimized geometry of the system with surface substitutional Fe doping (Fe@Ce₁), reported in Fig. 7a, results in more stable than the subsurface one (Fe@Ce₂) by 1.1 eV. The presence of such a Fe substitutional point defect induces a rearrangement of the neighboring O atoms. As a result, on the doped CeO₂ (111) surface, two non-equivalent O atoms (O₁ and O₄) and two equivalent (O₂=O₃) O sites are present, whereas in the subsurface layer all the O atoms (O₅, O₆ and O₇) results to be equivalent (see Fig. 7b). In this configuration, the Fe atom relaxes inward and binds to an O atom of the surface O₁, to three O atoms of the second layer O₅, O₆ and O₇, and to an O atom of the third layer O₈ (yellow O in Fig. 7b). The Fe-O bond lengths are found to be in the range of 1.84-2.14 Å, and therefore, corresponding to the distances in α - and γ -Fe₂O₃ (1.89-2.10 Å) [118]. In addition, the Bader charge of the substitutional Fe dopant is 14.28 e⁻ similar to those computed for the metal in α - and γ -Fe₂O₃ (14.34 and 14.49 e⁻). The Fe-O bond lengths of the five-coordinate moiety and the Bader charge calculations suggest that in our system the iron atom has an oxidation state of +3. In the doped surface, the Bader charges of the Ce atoms (9.6 e⁻) are consistent with the presence of Ce⁴⁺, indicating that no Ce⁴⁺ is reduced to Ce³⁺ in presence of the Fe dopant (see PDOS Fig. SI.10a). In the presence of a substitutional Fe atom in the CeO₂ system the computed value of the bandgap is 1.7 eV, thus 0.2 eV lower with respect to the undoped case, that is 1.9 eV (compare Fig. SI.10a and SI.10b).

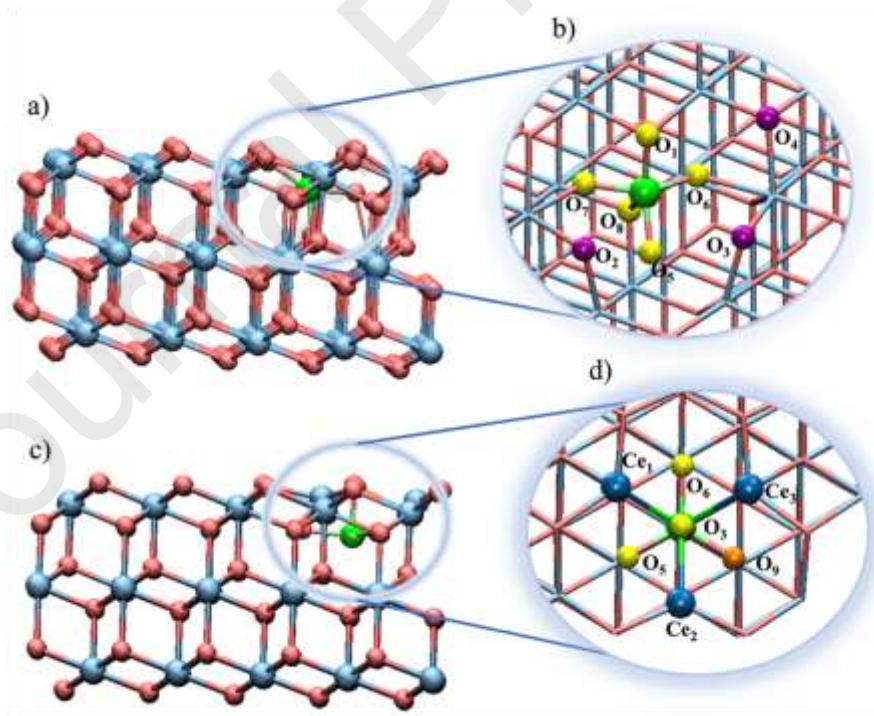


Fig. 7. Panel a) optimized structure of Fe@Ce₁ (111). Panel b) First and second coordination spheres of the Fe dopant. Ce, O, O_{1,5-8}, O₂₋₄ and Fe surface atoms are represented in balls and sticks and depicted in blue, red, yellow, purple and green, respectively. Panel c) optimized structure of Fe_{Int}.

Panel d) coordination sphere of the interstitial Fe dopant. Ce, O, O_{3,5,6}, O₉ and Fe surface atoms are represented in balls and sticks and depicted in blue, red, yellow, orange, and green, respectively.

Fig. 7.c shows the optimized structure of the Fe_{Int} system. Also in this case, the presence of the interstitial Fe dopant induces structural distortions on the surface. In fact, the Fe atom relaxes outward binding to the surface O₃ atoms and to the three O atoms of the second layer O₅, O₆ and O₉, (yellow and orange O in Fig. 7d). The formation of these new Fe-O bonds and the breaking of the pre-existing Ce-O bonds generates three reduced Ce³⁺. The Bader charges of these Ce atoms (9.9 e⁻) are consistent with the presence of Ce³⁺, also confirmed by the formation of two bandgap states below the Fermi level (black peaks in Fig. SI.11a of the SI) and by the spin density analysis, where the electron excess on the Ce³⁺ are indicated with black densities analogously to the colors of the respective bandgap peaks (Fig. SI.11c). In Fe_{Int} system the computed value of the bandgap is 1.7 eV similar to the substitutional Fe doping (compare Fig. SI.10a and SI.11a). For both doping types, the theoretical $\Delta\Delta E$ (eV) related to the band gap energy variation of the undoped and doped surfaces is in line with the experimentally calculated one and reported in Table 3.

Next, we have considered the formation of O vacancies on the most stable Fe@Ce₁ system. The presence of a Fe substitutional point defect generates four non-equivalent O atoms, namely O₁, O₂=O₃, O₄ in the outermost layer and O₅=O₆=O₇ in the subsurface layer, as discussed above (Fig. 7b). It is, therefore, possible to create four non-equivalent oxygen vacancies: VO₁, VO₂₌₃ and VO₄ in the external layer and VO₅₌₆₌₇ in the subsurface layer. The computed values of the formation energies (E_F) of VO₁, VO₂₌₃, VO₄ and VO₅₌₆₌₇ are found to be 0.7, 0.8, 2.13 and 1.1 eV, respectively. Our results show low formation energies for those oxygen vacancies arising from oxygen atoms directly coordinating or close enough to the Fe dopant (see VO₁, VO₂₌₃ and VO₅₌₆₌₇) and high E_F for those far from the iron atom. This occurs because the oxygen atoms very close to Fe are more affected by the structural distortions generated by the Fe dopant. The formation of a second oxygen vacancy VO₂ on the most stable reduced surface VO₁ (Fe@Ce₁:VO₁₋₂) is also favored, with an E_F of 0.9 eV, suggesting that the Fe dopant is likely the center of the oxygen vacancy cluster. A close inspection of the Bader charges, PDOS and spin density plots of the most stable Fe@Ce₁:VO₁ (111) system shows that the formation of an O vacancy leads to the reduction of two Ce⁴⁺ atoms that are formally Ce³⁺ (see Fig. SI.12).

To define the relative stability of the Fe-doped systems containing different types and or number of atoms depending on pressure and temperature, we have employed the formalism of ab initio thermodynamics as detailed described in the Experimental Section.

Fig. 8 shows a plot of the Gibbs energies $\Delta G_{ads}(T, p)$ of the system discussed above as a function of the O chemical potential including a conversion to oxygen partial pressures at several relevant temperatures. It is possible to identify three thermodynamically stable phases. The first phase, which holds for values of $\mu_o > -0.7$ eV, corresponds to the system where a Fe atom substitutes a surface Ce ion, Fe@Ce₁ (red line). Under O-rich conditions this structure becomes the thermodynamically most stable one. The second most stable structure is the one obtained by removing a surface O atom from the Fe@Ce₁ system (green line). This structure becomes thermodynamically stable in the range $-1.05 < \mu_o < -0.7$ eV (purple line). Finally, for $\mu_o < -1.05$ the Fe@Ce₁ system in the presence of two surface O vacancies becomes thermodynamically stable. These findings are in line with the experimental data suggesting that in the presence of Fe atoms substituting Ce ions the formation of O vacancies is favored. In addition, we predict that subsurface substitutional and interstitial Fe doping are never thermodynamically stable (blue and black lines, respectively).

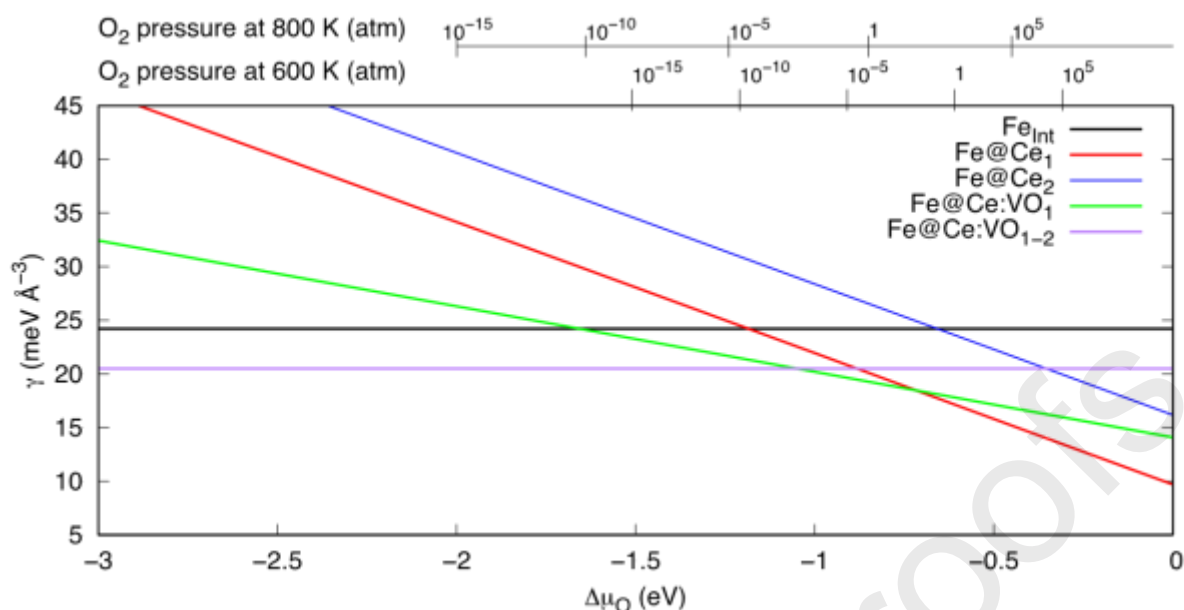


Fig. 8. Gibbs energies $\Delta G_{\text{ads}}(T, p)$ for substitutional, interstitial Fe atom in CeO_2 (111) and for reduced $\text{Fe@Ce}_1\text{:VO}_1$ and $\text{Fe@Ce}_1\text{:VO}_{1-2}$ (111) as a function of the oxygen chemical potential $\Delta\mu_{\text{O}}$ in eV.

3.3.2. Ibuprofen absorption on the surfaces

The interaction of IBU with stoichiometric (reduced) undoped CeO_2 (111) and the most stable Fe@Ce_1 surfaces was investigated, simulating IBU in its deprotonated form according to the experimental conditions.

Fig. 9 shows the optimized geometries of the most stable configurations of the IBU adsorbed on $\text{CeO}_2(111)$, Fe@Ce_1 (111), $\text{CeO}_2\text{:VO}_1(111)$, and $\text{Fe@Ce}_1\text{:VO}_1(111)$ (panel a-d, respectively).

IBU interacts with $\text{CeO}_2(111)$ through an ionic-like bond between an oxygen atom of its carboxylate group (O_{IBU}^1) and a surface Ce atom of 2.38 Å and an E_{ads} of -0.58 eV (Fig. 9a). In Fe@Ce_1 (111), the ligand binds the surface by a covalent-like bond between O_{IBU}^1 and the Fe dopant of 2.12 Å and an E_{ads} of -0.98 (Fig. 9b). In the stoichiometric system, the Fe dopant presence improves the adsorption energy of IBU by 0.4 eV due to i) the greater orbital availability of Fe^{3+} with respect to Ce^{4+} to host electrons and, thus, form new bonds and to ii) the structural distortions generated by the substitutional dopant. In fact, in the presence of Fe, the surface oxygen atom O_1 goes down towards the subsurface oxygen layer allowing a better interaction of the ligand with the Fe@Ce_1 (111) surface.

These energy stabilizations are also reflected in the reduced undoped and Fe-doped systems (Fig. 9c and 9d, respectively). The experiments are performed in aqueous solution and, therefore, water molecules will fill surface O vacancies of the ceria surface leading to a hydroxylated surface. However, if we assume that O vacancies are present on the catalysts, IBU molecules will adsorb on $\text{CeO}_2\text{:VO}_1$ (111) and $\text{Fe@Ce}_1\text{:VO}_1$ (111) through an ionic and covalent bond of 2.56 and 2.10 Å, respectively, and with E_{ads} of -2.28 and -2.43 eV for the undoped (panel c in Fig.9) and Fe-doped (panel d in Fig.9) reduced systems. Therefore, the hypothetical presence of the surface oxygen vacancy VO_1 improves the ligand E_{ads} of about 1.5 eV with respect to the stoichiometric surfaces as O_{IBU}^2 tends to occupy the vacant site stabilizing the IBU adsorption.

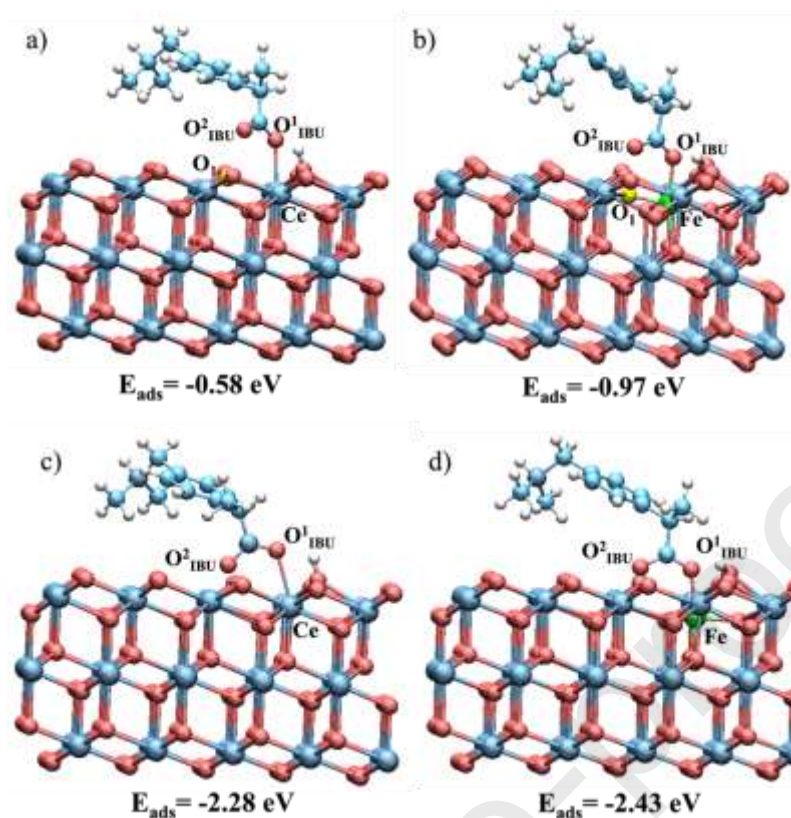


Fig. 9. Optimized structure of a) CeO_2 (111), b) Fe@Ce_1 (111), c) $\text{CeO}_2\text{@VO}_1$ (111) and d) $\text{Fe@Ce}_1\text{:VO}_1$ (111) with the corresponding E_{ads} (eV). Ce, O and O^{1-2} , O_1 , C, H and Fe surface atoms are represented in balls and sticks and depicted in blue, red, yellow, cyan, white and green, respectively.

3.4 Ibuprofen adsorption and photodegradation activity

Adsorption and photodegradation tests were conducted to investigate the performance of each synthesized catalyst. An attempt was made to justify the adsorption efficiency with the main properties of the catalysts. Except for the Fe10 sample, we do not observe any significant difference in terms of SSA and pore size. These findings lead us to speculate that the adsorption behaviour of IBU, except for Fe10, should not be determined by textural properties but could reflect differences in surface charge [93]. For this reason, the ζ -potential values at the pH of ibuprofen solution (pH=4.6), extrapolated from the ζ -potential curves (Fig. SI.13), were plotted vs the maximum adsorption capacity ($q_t = (C_{IBU,0} - C_{IBU})/\rho_B$), measured in dedicated experiments adopting the following experimental conditions: $T=30^\circ\text{C}$, $C_{IBU,0}=12.4\text{ mg L}^{-1}$, $\rho_B = 0.07\text{ g L}^{-1}$, reaction time of 300 min (Fig. 10a).

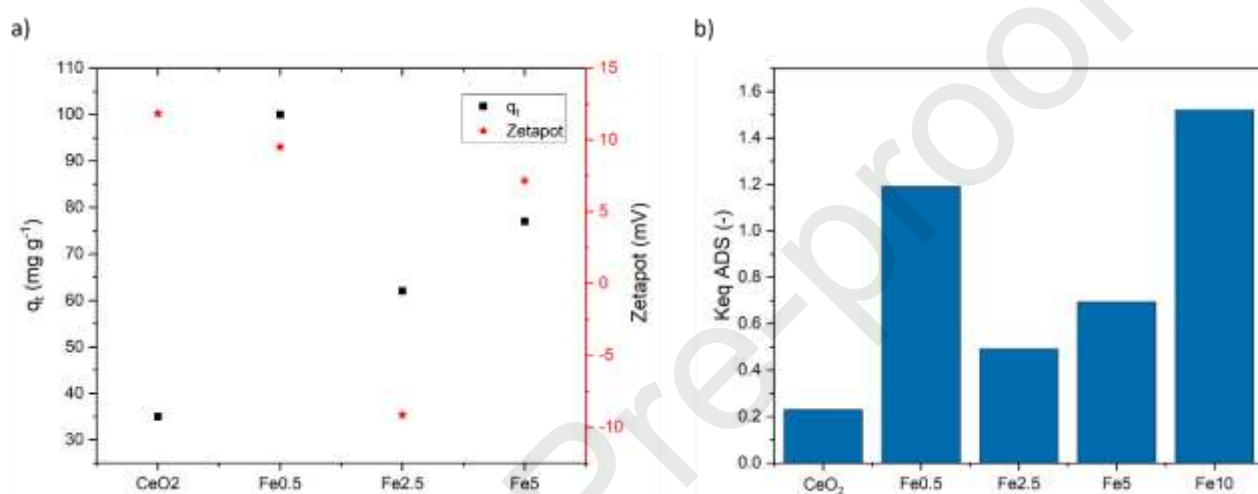


Fig. 10 – a) Potential (ζ) of the pristine and Fe-doped CeO₂ vs the adsorption capacity. b) Trend of the adsorption equilibrium constant. The present experimental conditions were adopted for each experiment: $T=30^\circ\text{C}$, $C_{IBU,0}=12.4\text{ mg L}^{-1}$, $\rho_B = 0.07\text{ g L}^{-1}$, reaction time of 300 min.

From the results shown in Fig. 10a, it is interesting to observe that Fe0.5 and Fe5 samples are positively charged at pH=4.6, namely the pH of the ibuprofen solution, while Fe2.5 is negatively charged. It is worth mentioning that the surface of both ceria and doped ceria is not “naked” but hydroxylated. Thus, being ibuprofen a weak acid (pK_a 4.41), in water it is partially dissociated in its anionic form. Therefore, the strongest interactions are expected to be with positively charged materials. Accordingly, the adsorption efficiency passes through a minimum for the Fe2.5 catalyst where the surface is negatively charged, inhibiting the ibuprofen adsorption. The different surface charge may be related to the type of hydroxyls exposed by Fe-CeO₂ surfaces, their distribution and their location with respect to oxygen vacancies [119,120].

The CeO₂ sample shows an opposite trend showing a very low adsorption efficiency even if the surface is positively charged, a finding not explainable by the above-mentioned hypothesis. But it is important to remind that from DFT computations (see Fig. 9), the adsorption energy of ibuprofen improves when it interacts with Fe rather than Ce, clearly leading to a lower adsorption efficiency compared with the samples containing Fe. As previously stated, the Fe10 sample is not included in the trend of doped samples discussion, because of its different properties such as very high surface area and the presence of surface oligomers (*vide supra*) that may promote higher adsorption efficiency. Furthermore, the type of adsorption was further evaluated by FT-IR spectroscopy. The

spectra obtained from the Fe2.5 sample and from the same sample after contact with a saturated ibuprofen solution are shown in Fig. SI.14. The spectra show a broad band between 3750 and 3000 cm^{-1} due to O-H stretching vibration of surface hydroxyl groups and undissociated water characterized by its bending mode at 1630 cm^{-1} [121,122]. Bands at around 1364 and 1529 cm^{-1} can be attributed to carbonate species, whose presence results from interactions of CeO_2 with atmospheric carbon dioxide [123]. Metal-oxygen vibration are generally observed at low wavenumbers, below 800 cm^{-1} . The absence of new chemical bonds in the post-saturation sample, inferred from the absence of new peaks in the saturated Fe2.5 catalyst, suggests a physisorption mechanism.

To measure the relative influence of adsorption and photodegradation contribution, the results were interpreted with a simplified kinetic model. The model was written taking into consideration a constant volume ideal batch reactor, where at the beginning of the reaction the ibuprofen solution is loaded to the vessel and the reaction is considered to occur in isothermal conditions. The rate expressions were developed, considering that ibuprofen (IBU) is adsorbed on the surface of the photocatalysts (*) leading to an adsorbed specie (IBU*), as in Eq. 2.



The reversible rate expression reported in Eq. 3 was adopted to describe the adsorption rate.

$$r_{\text{ADS}} = k_{\text{ADS}} \cdot \left(c_{\text{IBU}} - \frac{1}{K_{\text{eqADS}}} \cdot c_{\text{IBU}^*} \right) \quad (3)$$

The mentioned rate expression was included in the mass balance equation valid for a batch system, see Eq. 4.

$$\frac{dc_{\text{IBU}}}{dt} = -r_{\text{ADS}} \cdot \rho_B \quad (4)$$

The ordinary differential equation was solved in MATLAB R2023a environment, using *ode45* function, and the related adsorption kinetic and equilibrium constants were obtained by parameter estimation activity on the adsorption kinetic experiments. In detail, the objective function, defined as the square root of the squares of the residuals, was minimized using *lsqnonlin* algorithm. The results of the parameter estimation activities are reported in Figs 10b and Table 4.

As shown in Fig. 10b, the adsorption equilibrium constants follow the same trend as the adsorption capacity (q_t), being both quantities related to each other whose trend was previously explained via ζ -potential curves.

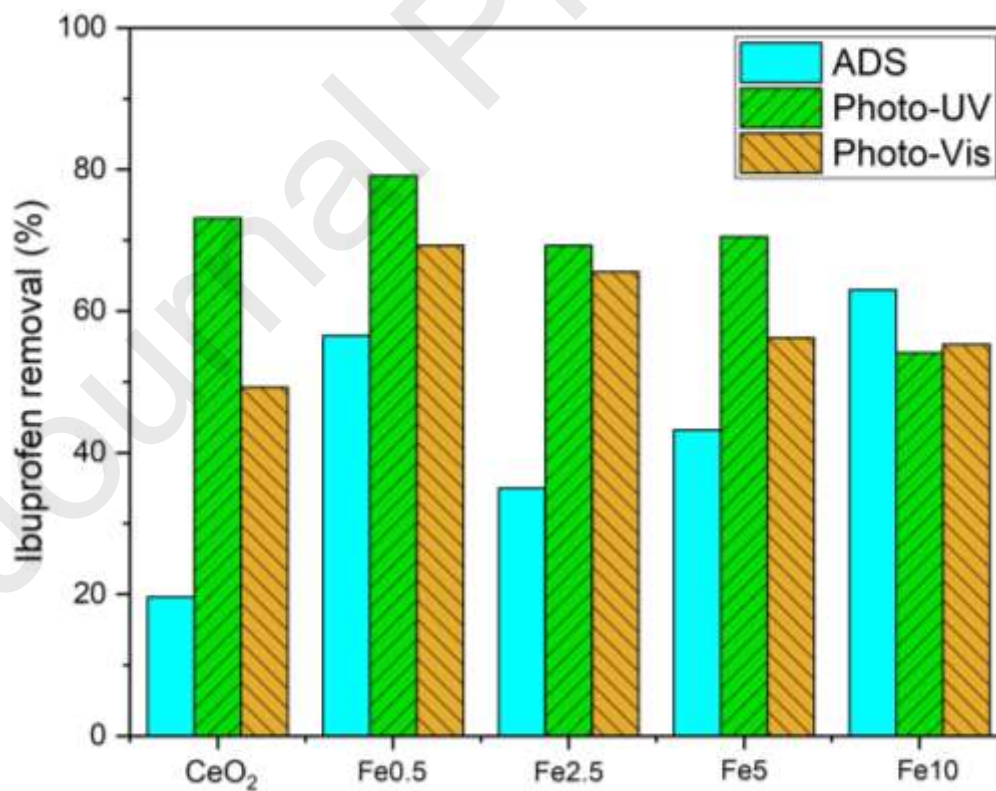
As adsorption is a physical phenomenon, its velocity depends on the effective diffusivity of ibuprofen molecules in the catalyst pores, thus the lumped kinetic constants reported in Table 4 are dependent on both the porosity and tortuosity of the catalysts. Being the pore volumes of each material very similar (see Table 3), the expected kinetic constants shall fall in the same range, as obtained by parameter estimation and reported in Table 4.

Table 4 – Adsorption rate, adsorption equilibrium and degradation rate constants values. The experimental conditions were adopted for each experiment: $T=30^\circ\text{C}$, $C_{\text{IBU},0}=12.4\text{mg L}^{-1}$, $\rho_B = 0.07\text{ g L}^{-1}$, reaction time of 300 min.

809

Sample	k_{ADS}	K_{eqADS}	k_{DEG}	
	($\text{L g}^{-1} \text{min}^{-1}$)	(-)	($\text{L g}^{-1} \text{min}^{-1}$)	
CeO₂	0.09 ± 0.02	0.23 ± 0.01	0.03 ± 0.01	photodegradation conducted either in or visible main results are where it is evident is slightly more visible irradiation The band gap value at the value of 3 eV allows the material the absorption of presence of iron in induces a shift in the in the studied reason, the doped more active under However, between UV and
Fe0.5	0.25 ± 0.01	1.19 ± 0.02	0.03 ± 0.01	
Fe2.5	0.16 ± 0.02	0.49 ± 0.02	0.11 ± 0.01	
Fe5	0.23 ± 0.02	0.69 ± 0.02	0.04 ± 0.01	
Fe10	0.37 ± 0.02	1.52 ± 0.03	0.0010 ± 0.0003	

performance
visible irradiation is a delicate balance of several factors, including band gap, surface defects and intra-band gap defect states (that can also act as recombination centres). The performance of the catalysts under visible irradiation is indeed promising for a scale-up process, considering the low lamp power and the used dosage of the catalysts.



832

833 **Fig. 11** –Trend of the ibuprofen removal percentage per each catalyst, under either dark or UV or VIS
 834 irradiation. The present experimental conditions were adopted for each experiment: $T=30^{\circ}\text{C}$, $C_{\text{IBU},0}=12.4 \text{ mg}$
 835 L^{-1} , $\rho_{\text{B}}=0.07 \text{ g L}^{-1}$, reaction time of 300 min.

836

837 Qualitatively, the best catalyst in terms of the overall removal of ibuprofen under visible irradiation
 838 is Fe0.5. Nevertheless, it is worth to be mentioned that during the photodegradation experiment, both
 839 adsorption and chemical reactions occur. For this reason, we have modified the aforementioned
 840 simplified mode, including a degradation step, described by the following rate expression.

$$841 \quad r_{DEG} = k_{DEG} \cdot c_{IBU^*} \quad (5)$$

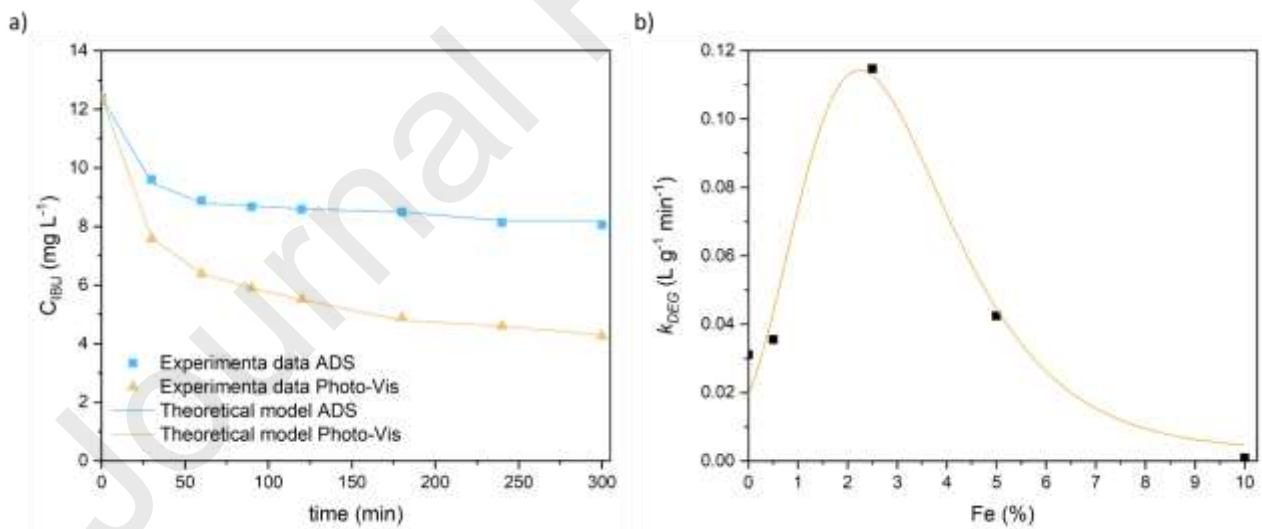
842 It must be pointed out, that we are implicitly assuming that photodegradation occurs in series to the
 843 adsorption process, while it could occur also in parallel. This simplification can be considered
 844 reasonable as we are interested in retrieving the order of magnitude of the kinetic constants to compare
 845 the activity of each catalyst. Further, the ibuprofen photolysis in the absence of the catalyst was
 846 neglected as proved experimentally [113].

847 Thus, the mass balance equation needs to be further modified, supposing that IBU* undergoes
 848 photodegradation, Eq. 6.

$$849 \quad \frac{dc_{IBU^*}}{dt} = (+r_{ADS} - r_{DEG}) \rho_B \quad (6)$$

850 In detail, Fig. 12a shows an example of data fit for the Fe2.5 catalyst: as revealed, a good fit was
 851 obtained both for adsorption and photodegradation experiments under visible irradiation. The results
 852 of the parameter estimation activities for all catalysts are reported in Table 4 and Fig. 12b.

853



854

855 **Fig. 12.** a) Example of data fit on the kinetic data measured using the Fe2.5 catalyst for both dark and
 856 photodegradation experiments under visible irradiation ($T=30^{\circ}C$, $C_{IBU,0}= 12.4 mg L^{-1}$, $\rho_B= 0.07 g L^{-1}$). Symbols represent the experimental data and lines the calculated profiles. b) Plot of the degradation
 857 constant as a function of Fe loading.
 858

859

860 Fig. 12b clearly illustrates that Fe2.5 is the best performing photocatalyst as it shows the highest
 861 degradation constant.

Raman and XPS findings revealed (*vide supra*) that Fe2.5 has the highest content of Ce³⁺ and defects-related oxygen vacancies. Raman results also suggested the highest charge delocalization for Fe2.5 (Fig. 4).

As extensively presented in the literature, the presence of oxygen vacancies can lead to increased photo-oxidation performance as they constitute trapping centres for photogenerated electrons, effectively limiting the rate of electron-hole recombination [124,125].

Finally, by comparing the band gap values with the degradation kinetic constant, it is possible to see that the activity passes through a maximum, as classically reported in the literature [126], thus it is possible to define an optimal band gap value of 2.79 eV (see Table 3).

For the mentioned reasons, it is interesting to further investigate the performance of Fe2.5 in terms of stability. Thus, reuse experiments were conducted under visible light irradiation. As reported in Fig. 13, the activity of Fe2.5 did not change after four cycles of photodegradation tests, demonstrating good stability, thus a potential use in continuous apparatus, allowing the scale-up of the process from batch to continuous operation.

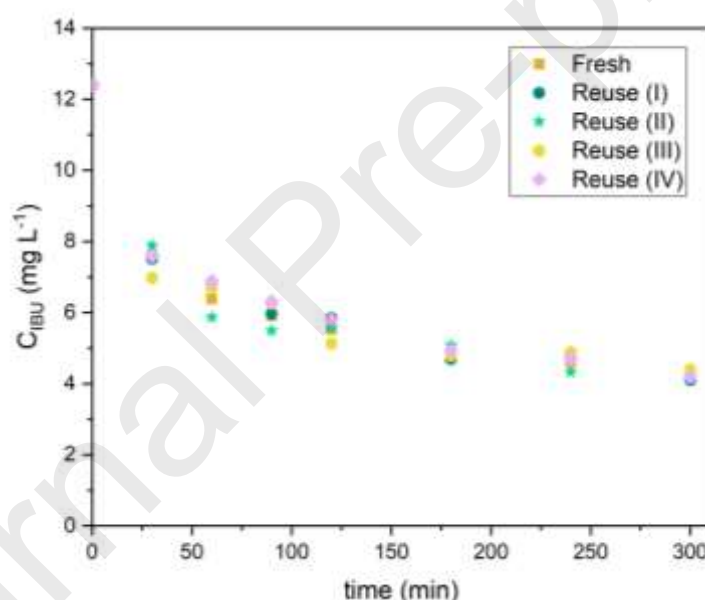


Fig. 13 – Reuse of the photocatalyst Fe2.5 in four photodegradation tests. The present experimental conditions were adopted for each experiment: $T = 30^{\circ}\text{C}$, $C_{\text{IBU},0} = 12.4 \text{ mg L}^{-1}$, $\rho_{\text{B}} = 0.07 \text{ g L}^{-1}$, reaction time of 300 min.

To further ascertain the stability of the catalyst, some relevant characterizations were conducted on the Fe2.5 sample after the reaction. The obtained results clearly showed no substantial changes in the nanocatalyst properties after the catalytic test. Indeed, the XRD diffraction pattern of the Fe2.5_post reaction (Fig SI.15a) shows the occurrence of the fluorite phase without any significant distortion of the structure.

Thermogravimetric analysis (Fig. SI.15b) analysis reports only a small variation on the region of chemisorbed water compared with the pristine catalyst, indicating that no organic by-products were adsorbed on the catalyst surface.

In accordance with XRD analysis, electron diffraction (see figure Fig. SI.15c) confirms that the cubic fluorite structure of the catalyst is retained after the catalytic tests and that no secondary crystalline phases are formed. The presence of Fe in the nanostructures is recognized by EDX analysis, with comparable EDX spectra (Fig. SI.15d) before and after the catalytic reaction. Moreover, based on HR-TEM images (Fig.SI.15e), it is interesting to notice that the catalytic reaction does not induce morphological or structural changes on the nanoparticles, which also preserve their characteristic size of approximately 5 nm.

Finally, XPS analysis performed on the sample post-catalysis shows first no contamination. Ce3d spectra obtained before and after photocatalysis are quite similar (Fig. SI.16a). A minor change of the v component (at 882.6 eV) can be seen, meaning that the Ce^{4+} contribution may have increased slightly. However, that variation is so small that it hardly affects its 3d3/2 counterpart. Consequently, in accordance with the other analyses, the XPS study confirms that the photocatalytic tests did not induce significant changes in the photocatalyst.

3.4 Identification of degradation by-products

A further objective of this work was the identification of possible degradation products.

The samples collected during the kinetic experiments were analysed via UV-Vis spectrophotometry and allowed the identification of an absorbance peak characteristic of an unknown chemical compound, at the wavelength $\lambda=260$ nm. Fig. 14 shows an example of the absorbance spectrum obtained at two different times, collected during a kinetic run conducted imposing the following reaction conditions: catalyst Fe2.5, $T=30^\circ\text{C}$, $C_{\text{IBU},0}=12.4\text{mg/L}$, $\rho_{\text{B}}=0.07\text{ g/L}$. In particular, the T0 sample was collected at time=0, while T1 at time = 30 min of reaction time.

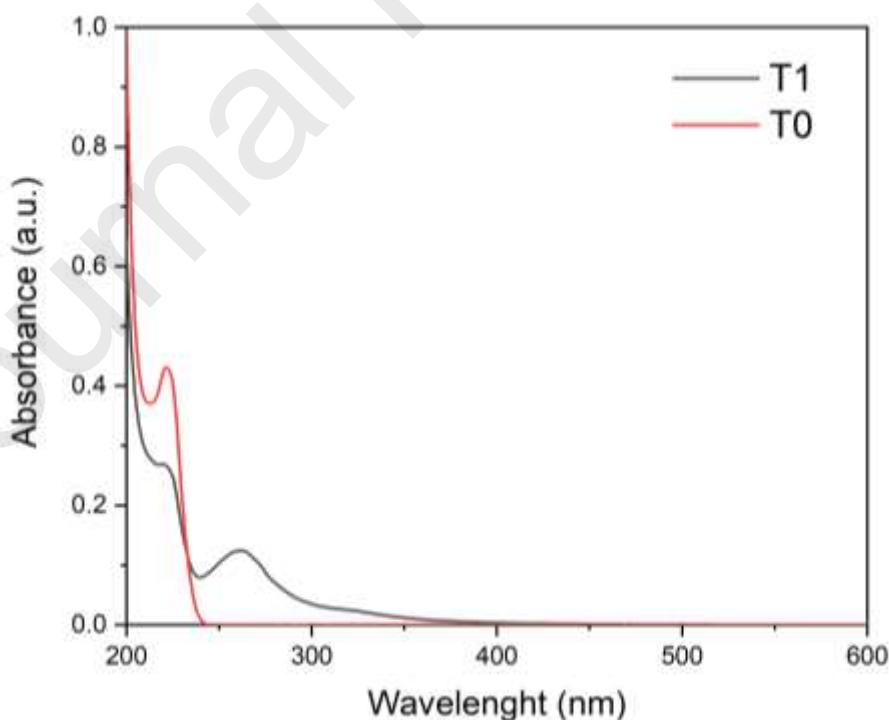


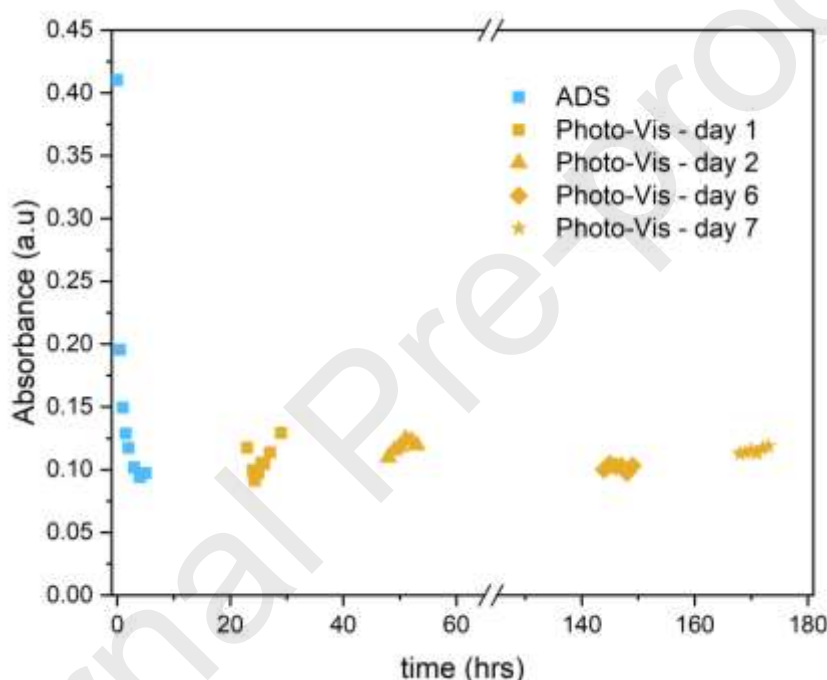
Fig. 14: Comparison between absorbance spectra of samples T0 (sample collected at time = 0) and T1 (sample collected at time = 30 min), collected during a kinetic run conducted imposing the following reaction conditions: catalyst Fe 2.5, $T=30^\circ\text{C}$, $C_{\text{IBU},0}=12.4\text{mg L}^{-1}$, $\rho_{\text{B}}=0.07\text{ g L}^{-1}$.

916

917 As Fig. 14 reveals, the peak at $\lambda=260$ nm is not present when analysing ibuprofen in water solution
 918 (T0). The additional peak was detected in every photodegradation test but with an absorbance variable
 919 with the experimental time. In particular, the absorbance increases as the reaction proceeds,
 920 simultaneously with the decrease of the absorbance measured at $\lambda=220$ nm.

921 Thus, it is important to carry out a more sophisticated analysis to understand the nature of the chemical
 922 compounds present during the photodegradation tests. The identification of the by-product generated
 923 by the reaction was conducted by performing an adsorption test and subsequent photodegradation.
 924 The samples were analysed using a UV-Vis spectrophotometer to monitor the absorbance peaks for
 925 ibuprofen and the by-products identified, further identified by LC-MS analysis.

926 The results obtained from the spectrophotometer analysis are shown in Fig. 15.



927

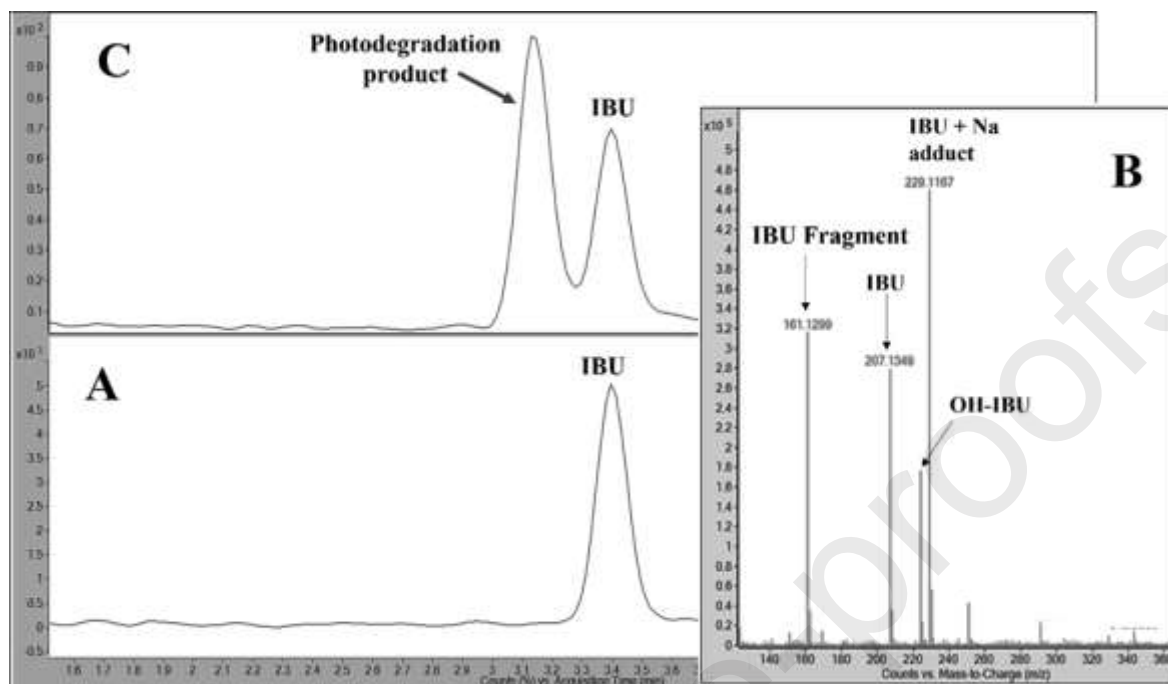
928 **Fig. 15:** Results obtained from spectrophotometer analyses. Experimental conditions: catalyst
 929 $\text{Fe}2.5$, $T = 30^\circ\text{C}$, $C_{\text{IBU},0} = 12.4 \text{ mg L}^{-1}$, $\rho_{\text{B}} = 0.07 \text{ g L}^{-1}$.

930

931 From the results reported in Fig. 15, it is possible to note that in dark, the absorbance recorded at the
 932 wavelength of $\lambda=220$ nm decreases, due to a decrease of ibuprofen concentration in the liquid solution
 933 due to the related adsorption on the catalyst. Starting from the first day of photodegradation, the
 934 absorbance measured at $\lambda=220$ nm remains constant for 7 days of reaction. The observed trend could
 935 be explained by the formation of by-products, showing an absorption at the same wavelength as
 936 ibuprofen.

937 The identification of neo-formed by-products obtained from the ibuprofen photodegradation was also
 938 performed by LC-MS analysis. The MS analysis was preliminarily performed on the standard solution
 939 (T0) of ibuprofen to set up the chromatographic conditions and MS parameters. The ion current of
 940 the chromatographic peak (3.4 min, Fig. 16 panel A) detected in the mixture at T0 was assigned to
 941 the molecular ion ($\text{M}+\text{H}^+$) of ibuprofen (IBU) at 207.1 m/z in addition to the hydroxylated form

942 (223.1 m/z) and the sodium adduct species (229.1 m/z) (Fig. 16, exploded panel B). Interestingly, an
 943 MS signal at 161.1 m/z was detected in the standard mixture (T0) due to the residue fragmentation
 944 occurring within the ESI source causing the loss of formic acid from the starting molecule.



945
 946 **Fig. 16:** Total ion current (TIC) chromatogram of the standard mixture (T0) (panel A) and the relative
 947 MS spectrum of peak at 3.4 min (panel B). TIC chromatogram of the mixture at the reaction time of
 948 24 h (T10) (panel C).

949
 950 Then, each aliquot analysed via UV-VIS spectrophotometry was further analysed via LC-TOF, to
 951 monitor the formation of the main by-products along the whole photodegradation experiment. The
 952 results reported in Fig. 17 demonstrated a marked decrease in ibuprofen after the first 30 min of
 953 reaction time (adsorption phase) followed by small variations of the peak area up to T10, Fig. 16
 954 panel C, (roughly 24 h of reaction) till reaching a constant value of roughly the 5% of the initial value
 955 (T0 sample) (Fig. 17).

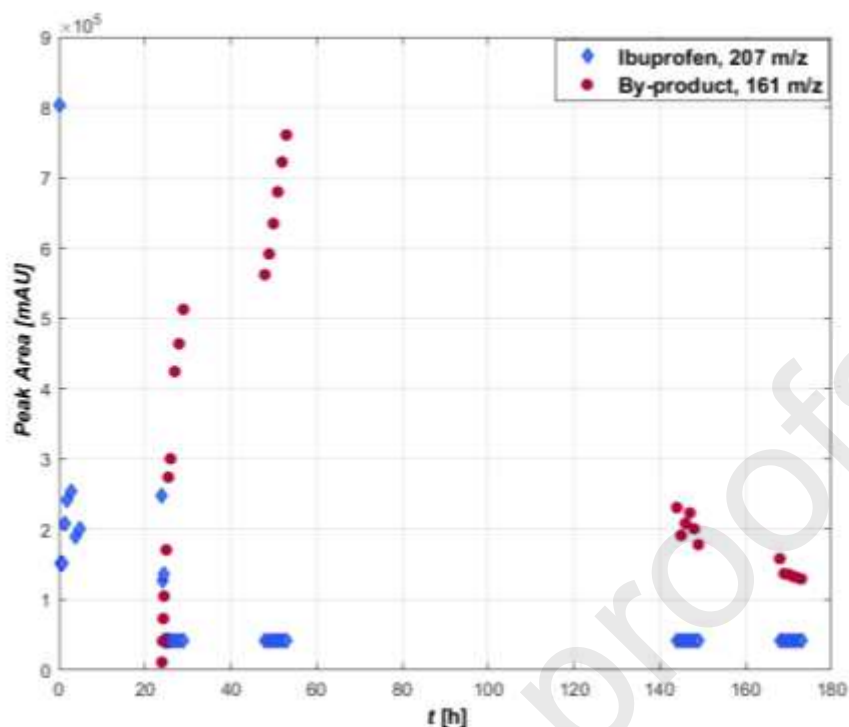
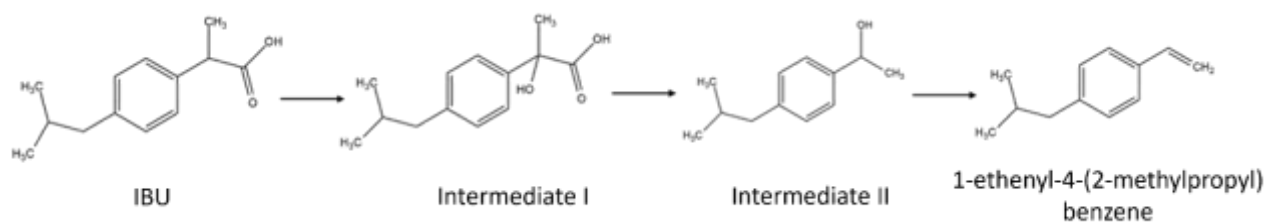


Fig. 17: Monitoring of kinetics of ibuprofen degradation and formation of by-products by mass spectrometry analysis.

The occurrence of neo-formed by-product started to appear at T8, corresponding to the start of the photodegradation step, displaying a chromatographic peak at a retention time shift of 0.3 min (3.1 min) from the intact ibuprofen. The identification of by-product at 161 m/z assigned to the 1-ethenyl-4-(2-methylpropyl)benzene ($C_{12}H_{16}$) was confirmed by GC-MS analysis where the fragments originated from the electron impact (IE) source were compared to the NIST database (Fig. SI.17).

Furthermore, a significant increase of by-product was observed up T23 (roughly after 2 days) where it reached the highest concentration. Then, after the second day, a drastic reduction of the product was recorded.

The presence of the mentioned by-product was already reported in the literature as possible intermediate in a more complex mechanism involving several degradation species. In particular, Rao et al., [127], reported that 1-ethenyl-4-(2-methylpropyl)benzene is produced by the dehydration and decomposition of two intermediates as described in Scheme 2. In the present work, the mentioned two intermediates were not detected, probably because the related reactions of formation and disappearance are relatively fast in the presence of Fe2.5 catalyst.



Scheme 2: Possible degradation pathway of IBU with formation of by-product detected in the present study.

Conclusions

Meticulous synthesis strategies for the preparation of robust and efficient photocatalysts are at the forefront of rapidly evolving fields, such as the removal of emerging contaminants in visible light-activated photocatalytic processes.

To avoid a trial and error approach we have selected a reliable and valuable bottom-up approach, the reverse micelle method, that allows to closely control the crystallographic and electronic properties of the ceria nanostructured photocatalysts. With controlled precipitation within the micelle nano-reactors, undoped and iron-substituted (0.50-10 mol %) ceria nanoparticles consisting of single crystals were successfully prepared. The sample with the highest iron content is the only one that shows the presence of oligomeric species on the surface while the other samples show an effective inclusion of substitutional iron in the ceria lattice.

The effect of the different iron content in the various samples revealed the role of iron heteroatoms in the delicate balance between adsorption and relative photodegradation of ibuprofen. Light was shed on the relationship between composition-structure and activity through numerous catalytic experiments, conducted both in the dark and under UV or visible irradiation. The results were supported by a combination of advanced characterisation techniques and DFT calculations, showing that the doping of the $\text{CeO}_2(111)$ surface with a substitutional Fe atom i) causes a decrease in the band gap of the system, improving the catalytic performance of the catalyst, ii) favours the formation of vacant sites (VOx) when the oxygen atoms are directly coordinated with the dopant or very close to it, iii) favours the IBU adsorption both in the stoichiometric and reduced model. Despite the presence of iron and vacancies being beneficial for ibuprofen adsorption, experimentally we find a non-linear trend of the adsorption capacity with the iron content. The latter was explained by measuring the z-potential of each sample, finding that adsorption is more efficient when the catalyst surface is positively charged. The combination of this effect and the non-linear trend of ibuprofen adsorption with Fe content leads to the identification of an optimal composition of the photocatalyst, namely 2.5 mol% Fe doped CeO_2 . The mentioned material showed good stability along 4 cycles of re-use experiments, demonstrating to be a promising material for a future application in flow.

Finally, GC-MS and HPLC-MS analyses were conducted on the samples collected in a dedicated experiment conducted with Fe2.5 catalyst under visible irradiation, allowing the identification of 1-ethenyl-4-(2-methylpropyl)benzene as the main by-product.

1013 **List of abbreviations***IBU* *Ibuprofen*

1014

()* *Free site*1015 **List of symbols***(IBU)* *Ibuprofen**(IBU*)* *Ibuprofen adsorbed into the solid**AOPs* *Advanced oxidation processes**NSAIDs* *Non-steroidal anti-inflammatory drugs**C_{IBU,0}* *ibuprofen initial concentration* *(mg L⁻¹)**C_{IBU}* *concentration of ibuprofen at t time* *(mg L⁻¹)**C_{IBU*}* *concentration of adsorbed ibuprofen* *(mg L⁻¹)**k_{ADS}* *adsorption kinetic constant* *(L (g min)⁻¹)**k_{DEG}* *desorption kinetic constant* *(L (g min)⁻¹)**K_{eqADS}* *adsorption constant* *(-)**qt* *adsorbed amount* *(mg g⁻¹)**r_{ADS}* *adsorption rate* *(mg g⁻¹ min⁻¹)**r_{DEG}* *desorption rate* *(mg g⁻¹ min⁻¹)**t* *time* *(min)**T* *temperature* *(°C)*

1016

1017 ***Greek symbol***

ρ_B sorbent bulk density (g L⁻¹)

1018

1019 **Acknowledgments**

1020 Miss Sonia Romano is cordially acknowledged for the experimental and numerical support given for
1021 the realization of the present study.

1022

1023 **Reference**

- 1024 1. Shah, A.H.; Rather, M.A.; Shah, A.H.; Rather, M.A. Advances in Nano Research. *Adv Nano Res* **2021**,
1025 10, 397, doi:10.12989/ANR.2021.10.4.397.
- 1026 2. Nath Bhadra, B.; Ahmed, I.; Kim, S.; Jhung, S.H. Adsorptive Removal of Ibuprofen and Diclofenac
1027 from Water Using Metal-Organic Framework-Derived Porous Carbon.,
1028 doi:10.1016/j.cej.2016.12.127.
- 1029 3. Madikizela, L.M.; Chimuka, L. Simultaneous Determination of Naproxen, Ibuprofen and Diclofenac in
1030 Wastewater Using Solid-Phase Extraction with High Performance Liquid Chromatography. *Water SA*
1031 **2017**, 43, 264, doi:10.4314/wsa.v43i2.10.
- 1032 4. Oba, S.N.; Ighalo, J.O.; Aniagor, C.O.; Igwegbe, A. Removal of Ibuprofen from Aqueous Media by
1033 Adsorption: A Comprehensive Review. *Science of the Total Environment* **2021**, 780, 146608,
1034 doi:10.1016/j.scitotenv.2021.146608.
- 1035 5. Ohtani, B. Photocatalysis A to Z-What We Know and What We Do Not Know in a Scientific Sense.
1036 *Journal of Photochemistry and Photobiology C: Photochemistry Reviews* **2010**, 11, 157–178,
1037 doi:10.1016/j.jphotochemrev.2011.02.001.
- 1038 6. Nan Chong, M.; Jin, B.; Chow, C.W.; Saint, C. Recent Developments in Photocatalytic Water
1039 Treatment Technology: A Review. *Water Res* **2010**, 44, 2997–3027,
1040 doi:10.1016/j.watres.2010.02.039.
- 1041 7. Melchionna, M.; Fornasiero, P. Updates on the Roadmap for Photocatalysis. **2020**,
1042 doi:10.1021/acscatal.0c01204.
- 1043 8. Mancuso, A.; Morante, N.; De Carluccio, M.; Sacco, O.; Rizzo, L.; Fontana, M.; Esposito, S.; Vaiano, V.;
1044 Sannino, D. Solar Driven Photocatalysis Using Iron and Chromium Doped TiO₂ Coupled to Moving
1045 Bed Biofilm Process for Olive Mill Wastewater Treatment. *Chemical Engineering Journal* **2022**, 450,
1046 138107, doi:10.1016/j.cej.2022.138107.
- 1047 9. Lou, L.; Wang, J.; Joon Lee, Y.; Ramkumar, S.S.; Lou, L.; Ramkumar, S.S.; Wang, J.; Lee, Y.J. Visible
1048 Light Photocatalytic Functional TiO₂/PVDF Nanofibers for Dye Pollutant Degradation. *Particle &*
1049 *Particle Systems Characterization* **2019**, 36, 1900091, doi:10.1002/PPSC.201900091.
- 1050 10. Iervolino, G.; Zammit, I.; Vaiano, V.; Rizzo, L. Limitations and Prospects for Wastewater Treatment by
1051 UV and Visible-Light-Active Heterogeneous Photocatalysis: A Critical Review. *Top Curr Chem* **2020**,
1052 378, 7, doi:10.1007/s41061-019-0272-1.
- 1053 11. Tammaro, O.; Morante, N.; Marocco, A.; Fontana, M.; Castellino, M.; Barrera, G.; Allia, P.; Tiberto,
1054 P.; Arletti, R.; Fantini, R.; et al. The Beneficial Role of Nano-Sized Fe₃O₄ Entrapped in Ultra-Stable Y
1055 Zeolite for the Complete Mineralization of Phenol by Heterogeneous Photo-Fenton under Solar
1056 Light. *Chemosphere* **2023**, 345, 140400, doi:10.1016/j.chemosphere.2023.140400.
- 1057 12. El-Sheikh, S.M.; Khedr, T.M.; Hakki, A.; Ismail, A.A.; Badawy, W.A.; Bahnemann, D.W. Visible Light
1058 Activated Carbon and Nitrogen Co-Doped Mesoporous TiO₂ as Efficient Photocatalyst for
1059 Degradation of Ibuprofen. *Sep Purif Technol* **2017**, 173, 258–268,
1060 doi:10.1016/J.SEPPUR.2016.09.034.
- 1061 13. Liu, N.; Wang, J.; Wu, J.; Li, Z.; Huang, W.; Zheng, Y.; Lei, J.; Zhang, X.; Tang, L. Magnetic Fe₃O₄
1062 @MIL-53(Fe) Nanocomposites Derived from MIL-53(Fe) for the Photocatalytic Degradation of
1063 Ibuprofen under Visible Light Irradiation. **2020**, doi:10.1016/j.materresbull.2020.111000.

- 1064 14. Sarafraz, M.; Amini, M.M.; Adiban, M.; Eslami, A. Facile Synthesis of Mesoporous Black N–TiO₂
1065 Photocatalyst for Efficient Charge Separation and the Visible-Driven Photocatalytic Mechanism of
1066 Ibuprofen Degradation. *Mater Sci Semicond Process* **2020**, *120*, 105258,
1067 doi:10.1016/J.MSSP.2020.105258.
- 1068 15. Liu, N.; Fei, F.; Dai, W.; Lei, J.; Bi, F.; Wang, B.; Quan, G.; Zhang, X.; Tang, L. Visible-Light-Assisted
1069 Persulfate Activation by SnS₂/MIL-88B(Fe) Z-Scheme Heterojunction for Enhanced Degradation of
1070 Ibuprofen. *J Colloid Interface Sci* **2022**, *625*, 965–977, doi:10.1016/J.JCIS.2022.06.099.
- 1071 16. Liu, N.; Wu, J.; Fei, F.; Lei, J.; Shi, W.; Quan, G.; Zeng, S.; Zhang, X.; Tang, L. Ibuprofen Degradation by
1072 a Synergism of Facet-Controlled MIL-88B(Fe) and Persulfate under Simulated Visible Light.,
1073 doi:10.1016/j.jcis.2021.12.142.
- 1074 17. Chaker, H.; Fourmentin, S.; Chérif-Aouali, L. Efficient Photocatalytic Degradation of Ibuprofen under
1075 Visible Light Irradiation Using Silver and Cerium Co-Doped Mesoporous TiO₂. *ChemistrySelect* **2020**,
1076 *5*, 11787–11796, doi:10.1002/slct.202002730.
- 1077 18. Montini, T.; Melchionna, M.; Monai, M.; Fornasiero, P. Fundamentals and Catalytic Applications of
1078 CeO₂-Based Materials. **2016**, doi:10.1021/acs.chemrev.5b00603.
- 1079 19. Mansingh, S.; Padhi, D.K.; Parida, K.M. Enhanced Photocatalytic Activity of Nanostructured Fe Doped
1080 CeO₂ for Hydrogen Production under Visible Light Irradiation. *Int J Hydrogen Energy* **2016**, *41*,
1081 14133–14146, doi:10.1016/j.ijhydene.2016.05.191.
- 1082 20. Corma, A.; Atienzar, P.; García, H.; Chane-Ching, J.-Y. Hierarchically Mesoporous Doped CeO₂
1083 with Potential for Solar-Cell Use. *Nat Mater* **2004**, *3*, 394–397, doi:10.1038/nmat1129.
- 1084 21. Kusmierek, E. A CeO₂ Semiconductor as a Photocatalytic and Photoelectrocatalytic Material for the
1085 Remediation of Pollutants in Industrial Wastewater: A Review. *Catalysts* **2020**, *10*, 1435,
1086 doi:10.3390/catal10121435.
- 1087 22. Ma, R.; Zhang, S.; Wen, T.; Gu, P.; Li, L.; Zhao, G.; Niu, F.; Huang, Q.; Tang, Z.; Wang, X. A Critical
1088 Review on Visible-Light-Response CeO₂-Based Photocatalysts with Enhanced Photooxidation of
1089 Organic Pollutants. *Catal Today* **2019**, *335*, 20–30, doi:10.1016/J.CATTOD.2018.11.016.
- 1090 23. Atran, A.A.; Hamdy, M.S. Improving the Photocatalytic Performance of Porous Ceria under Visible
1091 Light Illumination via Mn Incorporation. *Catalysts* **2023**, *13*, 523, doi:10.3390/catal13030523.
- 1092 24. Tsoncheva, T.; Rosmini, C.; Dimitrov, M.; Issa, G.; Henych, J.; Němečková, Z.; Kovacheva, D.; Velinov,
1093 N.; Atanasova, G.; Spassova, I. Formation of Catalytic Active Sites in Hydrothermally Obtained Binary
1094 Ceria-Iron Oxides: Composition and Preparation Effects. *ACS Appl Mater Interfaces* **2021**, *13*, 1838–
1095 1852, doi:10.1021/ACSAMI.0C16326/ASSET/IMAGES/LARGE/AM0C16326_0011.JPEG.
- 1096 25. Liu, B.; Yan, Z.; Xu, T.; Li, C.; Gao, R.; Hao, H.; Bai, J. Co-Construction of Oxygen Vacancies and
1097 Heterojunctions on CeO₂ via One-Step Fe Doping for Enhanced Photocatalytic Activity in Suzuki
1098 Reaction. *Chemical Engineering Journal* **2022**, *442*, 136226, doi:10.1016/J.CEJ.2022.136226.
- 1099 26. *Cerium Oxide (CeO₂): Synthesis, Properties and Applications*; Elsevier, 2020; ISBN 9780128156612.
- 1100 27. Younis, A.; Chu, D.; Kaneti, Y.V.; Li, S. Tuning the Surface Oxygen Concentration of {111} Surrounded
1101 Ceria Nanocrystals for Enhanced Photocatalytic Activities. *Nanoscale* **2015**, *8*, 378–387,
1102 doi:10.1039/C5NR06588G.

- 1103 28. Choudhury, B.; Chetri, P.; Choudhury, A. Oxygen Defects and Formation of Ce³⁺ Affecting the
1104 Photocatalytic Performance of CeO₂ Nanoparticles. *RSC Adv* **2013**, *4*, 4663–4671,
1105 doi:10.1039/C3RA44603D.
- 1106 29. Trovarelli, A. Structural and Oxygen Storage/Release Properties of CeO₂-Based Solid Solutions.
1107 *Comments on Inorganic Chemistry* **1999**, *20*, 263–284, doi:10.1080/02603599908021446.
- 1108 30. TROVARELLI, A. Catalytic Properties of Ceria and CeO₂-Containing Materials. *Catalysis Reviews*
1109 **1996**, *38*, 439–520, doi:10.1080/01614949608006464.
- 1110 31. Zhang, F.; Zhao, L.; Chen, H.; He, Y.; Tian, P.; Zeng, X. Synthesis of Mesoporous Fe/h-CeO₂ Hollow
1111 Micro-Spheres with Enhanced Visible Light Photocatalytic Activity. *Mater Res Express* **2019**, *6*,
1112 095516, doi:10.1088/2053-1591/ab3015.
- 1113 32. Cai, W.; Chen, F.; Shen, X.; Chen, L.; Zhang, J. Enhanced Catalytic Degradation of AO7 in the CeO₂-
1114 H₂O₂ System with Fe³⁺ Doping. *Appl Catal B* **2010**, *101*, 160–168,
1115 doi:10.1016/j.apcatb.2010.09.031.
- 1116 33. Channei, D.; Inceesungvorn, B.; Wetchakun, N.; Ukritnukun, S.; Nattestad, A.; Chen, J.;
1117 Phanichphant, S. Photocatalytic Degradation of Methyl Orange by CeO₂ and Fe-Doped CeO₂ Films
1118 under Visible Light Irradiation. *Sci Rep* **2014**, *4*, 5757, doi:10.1038/srep05757.
- 1119 34. Zhao, B.; Shao, Q.; Hao, L.; Zhang, L.; Liu, Z.; Zhang, B.; Ge, S.; Guo, Z. Yeast-Template Synthesized
1120 Fe-Doped Cerium Oxide Hollow Microspheres for Visible Photodegradation of Acid Orange 7. *J*
1121 *Colloid Interface Sci* **2018**, *511*, 39–47, doi:10.1016/j.jcis.2017.09.077.
- 1122 35. Wang, Y.; Wang, F.; Chen, Y.; Zhang, D.; Li, B.; Kang, S.; Li, X.; Cui, L. Enhanced Photocatalytic
1123 Performance of Ordered Mesoporous Fe-Doped CeO₂ Catalysts for the Reduction of CO₂ with H₂O
1124 under Simulated Solar Irradiation. *Appl Catal B* **2014**, *147*, 602–609,
1125 doi:10.1016/j.apcatb.2013.09.036.
- 1126 36. Channei, D.; Inceesungvorn, B.; Wetchakun, N.; Phanichphant, S.; Nakaruk, A.; Koshy, P.; Sorrell, C.C.
1127 Photocatalytic Activity under Visible Light of Fe-Doped CeO₂ Nanoparticles Synthesized by Flame
1128 Spray Pyrolysis. *Ceram Int* **2013**, *39*, 3129–3134, doi:10.1016/j.ceramint.2012.09.093.
- 1129 37. Esposito, S. Introduction. In *Sol-Gel Synthesis Strategies for Tailored Catalytic Materials* ; 2023; pp.
1130 1–12, https://doi.org/10.1007/978-3-031-20723-5_1.
- 1131 38. Pileni, M.P. Reverse Micelles as Microreactors. *J Phys Chem* **1993**, *97*, 6961–6973,
1132 doi:10.1021/j100129a008.
- 1133 39. Moragues, T.; Arguijo, D.; Beneyton, T.; Modavi, C.; Simutis, K.; Abate, A.R.; Baret, J.-C.; deMello,
1134 A.J.; Densmore, D.; Griffiths, A.D. Droplet-Based Microfluidics. *Nature Reviews Methods Primers*
1135 **2023**, *3*, 32, doi:10.1038/s43586-023-00212-3.
- 1136 40. Omid, M.; Almeida, L.; Tayebi, L. Microfluidic-assisted Fabrication of Reverse Micelle/PLGA Hybrid
1137 Microspheres for Sustained Vascular Endothelial Growth Factor Delivery. *Biotechnol Appl Biochem*
1138 **2021**, *68*, 616–625, doi:10.1002/bab.1971.
- 1139 41. Quinlan, F.T.; Kuther, J.; Tremel, W.; Knoll, W.; Risbud, S.; Stroeve, P. Reverse Micelle Synthesis and
1140 Characterization of ZnSe Nanoparticles. *Langmuir* **2000**, *16*, 4049–4051, doi:10.1021/la9909291.
- 1141 42. Morrison, S.A.; Cahill, C.L.; Carpenter, E.E.; Harris, V.G. Production Scaleup of Reverse Micelle
1142 Synthesis. *Ind Eng Chem Res* **2006**, *45*, 1217–1220, doi:10.1021/ie050886l.

- 1143 43. Tammaro, O.; Costagliola di Polidoro, A.; Romano, E.; Netti, P.A.; Torino, E. A Microfluidic Platform
1144 to Design Multimodal PEG - Crosslinked Hyaluronic Acid Nanoparticles (PEG-CHANPs) for Diagnostic
1145 Applications. *Sci Rep* **2020**, *10*, doi:10.1038/s41598-020-63234-x.
- 1146 44. Lee, Y.; Lee, J.; Bae, C.J.; Park, J.-G.; Noh, H.-J.; Park, J.-H.; Hyeon, T. Large-Scale Synthesis of Uniform
1147 and Crystalline Magnetite Nanoparticles Using Reverse Micelles as Nanoreactors under Reflux
1148 Conditions. *Adv Funct Mater* **2005**, *15*, 503–509, doi:10.1002/adfm.200400187.
- 1149 45. Arsene, M.-L.; Răut, I.; Călin, M.; Jecu, M.-L.; Doni, M.; Gurban, A.-M. Versatility of Reverse Micelles:
1150 From Biomimetic Models to Nano (Bio)Sensor Design. *Processes* **2021**, *9*, 345,
1151 doi:10.3390/pr9020345.
- 1152 46. Laguna, O.H.; Centeno, M.A.; Boutonnet, M.; Odriozola, J.A. Fe-Doped Ceria Solids Synthesized by
1153 the Microemulsion Method for CO Oxidation Reactions. *Appl Catal B* **2011**, *106*, 621–629,
1154 doi:10.1016/j.apcatb.2011.06.025.
- 1155 47. Pournajaf, R.; Hassanzadeh-Tabrizi, S.A.; Jafari, M. Reverse Microemulsion Synthesis of CeO₂
1156 Nanopowder Using Polyoxyethylene(23)Lauryl Ether as a Surfactant. *Ceram Int* **2014**, *40*, 8687–
1157 8692, doi:10.1016/j.ceramint.2014.01.086.
- 1158 48. Tescione, F.; Tammaro, O.; Bifulco, A.; Del Monaco, G.; Esposito, S.; Pansini, M.; Silvestri, B.;
1159 Costantini, A. Silica Meets Tannic Acid: Designing Green Nanoplatfoms for Environment
1160 Preservation. *Molecules* **2022**, *27*, 1944, doi:10.3390/molecules27061944.
- 1161 49. Addorisio, V.; Pirozzi, D.; Esposito, S.; Sannino, F. Decontamination of Waters Polluted with Simazine
1162 by Sorption on Mesoporous Metal Oxides. *J Hazard Mater* **2011**, *196*, 242–247,
1163 doi:10.1016/j.jhazmat.2011.09.022.
- 1164 50. Perdew, J.P.; Burke, K.; Ernzerhof, M. Generalized Gradient Approximation Made Simple. *Phys Rev*
1165 *Lett* **1996**, *77*, 3865–3868, doi:10.1103/PhysRevLett.77.3865.
- 1166 51. Vanderbilt, D. Soft Self-Consistent Pseudopotentials in a Generalized Eigenvalue Formalism. *Phys*
1167 *Rev B* **1990**, *41*, 7892–7895, doi:10.1103/PhysRevB.41.7892.
- 1168 52. Giannozzi, P.; Andreussi, O.; Brumme, T.; Bunau, O.; Buongiorno Nardelli, M.; Calandra, M.; Car, R.;
1169 Cavazzoni, C.; Ceresoli, D.; Cococcioni, M.; et al. Advanced Capabilities for Materials Modelling with
1170 Quantum ESPRESSO. *Journal of Physics: Condensed Matter* **2017**, *29*, 465901, doi:10.1088/1361-
1171 648X/aa8f79.
- 1172 53. Cococcioni, M.; de Gironcoli, S. Linear Response Approach to the Calculation of the Effective
1173 Interaction Parameters in the $\langle \text{LDA} \rangle$ Method. *Phys Rev B* **2005**, *71*, 035105,
1174 doi:10.1103/PhysRevB.71.035105.
- 1176 54. Loschen, C.; Carrasco, J.; Neyman, K.M.; Illas, F. First-Principles $\langle \text{LDA} \rangle$ and $\langle \text{GGA} \rangle$
1177 $\langle \text{LDA} \rangle$ and $\langle \text{GGA} \rangle$ Study of Cerium Oxides: Dependence on the Effective U Parameter. *Phys Rev B*
1178 **2007**, *75*, 035115, doi:10.1103/PhysRevB.75.035115.
- 1181 55. Fabris, S.; Vicario, G.; Balducci, G.; de Gironcoli, S.; Baroni, S. Electronic and Atomistic Structures of
1182 Clean and Reduced Ceria Surfaces. *J Phys Chem B* **2005**, *109*, 22860–22867, doi:10.1021/jp0511698.

- 1183 56. Nolan, M.; Grigoleit, S.; Sayle, D.C.; Parker, S.C.; Watson, G.W. Density Functional Theory Studies of
1184 the Structure and Electronic Structure of Pure and Defective Low Index Surfaces of Ceria. *Surf Sci*
1185 **2005**, 576, 217–229, doi:10.1016/j.susc.2004.12.016.
- 1186 57. Nolan, M.; Watson, G.W. The Surface Dependence of CO Adsorption on Ceria. *J Phys Chem B* **2006**,
1187 110, 16600–16606, doi:10.1021/jp062499a.
- 1188 58. Da Silva, J.L.F.; Ganduglia-Pirovano, M.V.; Sauer, J.; Bayer, V.; Kresse, G. Hybrid Functionals Applied
1189 to Rare-Earth Oxides: The Example of Ceria. *Phys Rev B* **2007**, 75, 045121,
1190 doi:10.1103/PhysRevB.75.045121.
- 1191 59. Zhang, C.; Michaelides, A.; King, D.A.; Jenkins, S.J. Structure of Gold Atoms on Stoichiometric and
1192 Defective Ceria Surfaces. *J Chem Phys* **2008**, 129, 194708, doi:10.1063/1.3009629.
- 1193 60. Yue, L.; Zhang, X.-M. Structural Characterization and Photocatalytic Behaviors of Doped CeO₂
1194 Nanoparticles. *J Alloys Compd* **2009**, 475, 702–705, doi:10.1016/j.jallcom.2008.07.096.
- 1195 61. Ganduglia-Pirovano, M.V.; Da Silva, J.L.F.; Sauer, J. Density-Functional Calculations of the Structure
1196 of Near-Surface Oxygen Vacancies and Electron Localization on CeO_2/Mn . *Phys Rev Lett* **2009**, 102, 026101,
1197 doi:10.1103/PhysRevLett.102.026101.
- 1200 62. Szabová, L.; Camellone, M.F.; Huang, M.; Matolín, V.; Fabris, S. Thermodynamic, Electronic and
1201 Structural Properties of Cu/CeO₂ Surfaces and Interfaces from First-Principles DFT+U Calculations. *J*
1202 *Chem Phys* **2010**, 133, 234705, doi:10.1063/1.3515424.
- 1203 63. Chen, A.; Yu, X.; Zhou, Y.; Miao, S.; Li, Y.; Kuld, S.; Sehested, J.; Liu, J.; Aoki, T.; Hong, S.; et al.
1204 Structure of the Catalytically Active Copper–Ceria Interfacial Perimeter. *Nat Catal* **2019**, 2, 334–341,
1205 doi:10.1038/s41929-019-0226-6.
- 1206 64. Tran, N.-D.; Farnesi Camellone, M.; Fabris, S. Probing the Reactivity of Pt/Ceria Nanocatalysts toward
1207 Methanol Oxidation: From Ionic Single-Atom Sites to Metallic Nanoparticles. *The Journal of Physical*
1208 *Chemistry C* **2018**, 122, 17917–17927, doi:10.1021/acs.jpcc.8b05735.
- 1209 65. Dvořák, F.; Szabová, L.; Johánek, V.; Farnesi Camellone, M.; Stetsovych, V.; Vorokhta, M.; Tovt, A.;
1210 Skála, T.; Matolínová, I.; Tateyama, Y.; et al. Bulk Hydroxylation and Effective Water Splitting by
1211 Highly Reduced Cerium Oxide: The Role of O Vacancy Coordination. *ACS Catal* **2018**, 8, 4354–4363,
1212 doi:10.1021/acscatal.7b04409.
- 1213 66. Oh, S.; Shin, W.S.; Kim, H.T. Effects of PH, Dissolved Organic Matter, and Salinity on Ibuprofen
1214 Sorption on Sediment. *Environmental Science and Pollution Research* **2016**, 23, 22882–22889,
1215 doi:10.1007/s11356-016-7503-6.
- 1216 67. Ritacco, I.; Imparato, C.; Falivene, L.; Cavallo, L.; Magistrato, A.; Caporaso, L.; Farnesi Camellone, M.;
1217 Aronne, A. Spontaneous Production of Ultrastable Reactive Oxygen Species on Titanium Oxide
1218 Surfaces Modified with Organic Ligands. *Adv Mater Interfaces* **2021**, 8, 2100629,
1219 doi:10.1002/admi.202100629.
- 1220 68. Finkelstein-Shapiro, D.; Davidowski, S.K.; Lee, P.B.; Guo, C.; Holland, G.P.; Rajh, T.; Gray, K.A.; Yarger,
1221 J.L.; Calatayud, M. Direct Evidence of Chelated Geometry of Catechol on TiO₂ by a Combined Solid-
1222 State NMR and DFT Study. *The Journal of Physical Chemistry C* **2016**, 120, 23625–23630,
1223 doi:10.1021/acs.jpcc.6b08041.

- 1224 69. Liu, L.-M.; Li, S.-C.; Cheng, H.; Diebold, U.; Selloni, A. Growth and Organization of an Organic
1225 Molecular Monolayer on TiO_2 : Catechol on Anatase (101). *J Am Chem Soc* **2011**, *133*, 7816–7823,
1226 doi:10.1021/ja200001r.
- 1227 70. Guo, L.; Huang, Y.; Ritacca, A.G.; Wang, K.; Ritacco, I.; Tan, Y.; Qiang, Y.; Al-Zaqri, N.; Shi, W.; Zheng,
1228 X. Effect of Indole-2-Carboxylic Acid on the Self-Corrosion and Discharge Activity of Aluminum Alloy
1229 Anode in Alkaline Al–Air Battery. *Molecules* **2023**, *28*, 4193, doi:10.3390/molecules28104193.
- 1230 71. Kaxiras, E.; Bar-Yam, Y.; Joannopoulos, J.D.; Pandey, K.C. *Ab Initio* Theory of Polar Semiconductor
1231 Surfaces. I. Methodology and the (22) Reconstructions of GaAs(111). *Phys Rev B* **1987**, *35*, 9625–
1232 9635, doi:10.1103/PhysRevB.35.9625.
- 1233 72. Qian, G.-X.; Martin, R.M.; Chadi, D.J. First-Principles Study of the Atomic Reconstructions and
1234 Energies of Ga- and As-Stabilized GaAs(100) Surfaces. *Phys Rev B* **1988**, *38*, 7649–7663,
1235 doi:10.1103/PhysRevB.38.7649.
- 1236 73. Reuter, K.; Scheffler, M. Composition, Structure, and Stability of $\text{RuO}_2/\text{MnO}_2$ as a
1237 $\text{RuO}_2/\text{MnO}_2$ as a
1238 $\text{RuO}_2/\text{MnO}_2$ as a
1239 Function of Oxygen Pressure. *Phys Rev B* **2001**, *65*, 035406, doi:10.1103/PhysRevB.65.035406.
- 1240 74. Meyer, B. First-Principles Study of the Polar O-Terminated ZnO Surface in Thermodynamic
1241 Equilibrium with Oxygen and Hydrogen. *Phys Rev B* **2004**, *69*, 045416,
1242 doi:10.1103/PhysRevB.69.045416.
- 1243 75. Henkelman, G.; Arnaldsson, A.; Jónsson, H. A Fast and Robust Algorithm for Bader Decomposition of
1244 Charge Density. *Comput Mater Sci* **2006**, *36*, 354–360, doi:10.1016/j.commatsci.2005.04.010.
- 1245 76. Sanville, E.; Kenny, S.D.; Smith, R.; Henkelman, G. Improved Grid-Based Algorithm for Bader Charge
1246 Allocation. *J Comput Chem* **2007**, *28*, 899–908, doi:10.1002/jcc.20575.
- 1247 77. Tang, W.; Sanville, E.; Henkelman, G. A Grid-Based Bader Analysis Algorithm without Lattice Bias.
1248 *Journal of Physics: Condensed Matter* **2009**, *21*, 084204, doi:10.1088/0953-8984/21/8/084204.
- 1249 78. Friuli, V.; Bruni, G.; Musitelli, G.; Conte, U.; Maggi, L. Influence of Dissolution Media and Presence of
1250 Alcohol on the In Vitro Performance of Pharmaceutical Products Containing an Insoluble Drug. *J*
1251 *Pharm Sci* **2018**, *107*, 507–511, doi:10.1016/j.xphs.2017.06.001.
- 1252 79. Esposito, S.; Silvestri, B.; Russo, V.; Bonelli, B.; Manzoli, M.; Deorsola, F.A.; Vergara, A.; Aronne, A.; Di
1253 Serio, M. Self-Activating Catalyst for Glucose Hydrogenation in the Aqueous Phase under Mild
1254 Conditions. *ACS Catal* **2019**, *9*, 3426–3436, doi:10.1021/acscatal.8b04710.
- 1255 80. Esposito, S. Evolution of Sol–Gel Chemistry. In *Sol-Gel Synthesis Strategies for Tailored Catalytic*
1256 *Materials*; Springer International Publishing: Cham, 2023; pp. 43–51 ISBN 978-3-031-20722-8,
1257 https://doi.org/10.1007/978-3-031-20723-5_5.
- 1258 81. Bonelli, B.; Tammara, O.; Martinovic, F.; Nasi, R.; Dell’Agli, G.; Rivolo, P.; Giorgis, F.; Ditaranto, N.;
1259 Deorsola, F.A.; Esposito, S. Reverse Micelle Strategy for the Synthesis of $\text{MnO}_x\text{–TiO}_2$ Active
1260 Catalysts for NH_3 -Selective Catalytic Reduction of NO_x at Both Low Temperature and Low Mn
1261 Content. *ACS Omega* **2021**, *6*, 24562–24574, doi:10.1021/acsomega.1c03153.
- 1262 82. Nasi, R.; Esposito, S.; Freyria, F.; Armandi, M.; Gadhi, T.; Hernandez, S.; Rivolo, P.; Ditaranto, N.;
1263 Bonelli, B. Application of Reverse Micelle Sol–Gel Synthesis for Bulk Doping and Heteroatoms

- 1264 Surface Enrichment in Mo-Doped TiO₂ Nanoparticles. *Materials* **2019**, *12*, 937,
1265 doi:10.3390/ma12060937.
- 1266 83. Mancuso, A.; Blangetti, N.; Sacco, O.; Freyria, F.S.; Bonelli, B.; Esposito, S.; Sannino, D.; Vaiano, V.
1267 Photocatalytic Degradation of Crystal Violet Dye under Visible Light by Fe-Doped TiO₂ Prepared by
1268 Reverse-Micelle Sol–Gel Method. *Nanomaterials* **2023**, *13*, 270, doi:10.3390/nano13020270.
- 1269 84. Esposito, S. Synthetic Strategies for (Supported) Metal and Metal Oxide Catalysts: Case Studies. In
1270 *Sol-Gel Synthesis Strategies for Tailored Catalytic Materials*; 2023; pp. 53–71,
1271 https://doi.org/10.1007/978-3-031-20723-5_6.
- 1272 85. Malik, M.A.; Wani, M.Y.; Hashim, M.A. Microemulsion Method: A Novel Route to Synthesize Organic
1273 and Inorganic Nanomaterials. *Arabian Journal of Chemistry* **2012**, *5*, 397–417,
1274 doi:10.1016/j.arabjc.2010.09.027.
- 1275 86. Water in and around Micelles, Reverse Micelles, and Microemulsions. In *Water in Biological and*
1276 *Chemical Processes*; Cambridge University Press, 2013; pp. 261–276.
- 1277 87. Choudhury, B.; Chetri, P.; Choudhury, A. Oxygen Defects and Formation of Ce³⁺ Affecting the
1278 Photocatalytic Performance of CeO₂ Nanoparticles. *RSC Adv.* **2014**, *4*, 4663–4671,
1279 doi:10.1039/C3RA44603D.
- 1280 88. Shih, S.-J.; Wu, Y.-Y.; Chen, C.-Y.; Yu, C.-Y. Morphology and Formation Mechanism of Ceria
1281 Nanoparticles by Spray Pyrolysis. *Journal of Nanoparticle Research* **2012**, *14*, 879,
1282 doi:10.1007/s11051-012-0879-4.
- 1283 89. Anghel, E.M.; Petrescu, S.; Mocioiu, O.C.; Cusu, J.P.; Atkinson, I. Influence of Ceria Addition on
1284 Crystallization Behavior and Properties of Mesoporous Bioactive Glasses in the SiO₂–CaO–P₂O₅–
1285 CeO₂ System. *Gels* **2022**, *8*, 344, doi:10.3390/gels8060344.
- 1286 90. Woan, K.; Tsai, Y.-Y.; Sigmund, W. Synthesis and Characterization of Luminescent Cerium Oxide
1287 Nanoparticles. *Nanomedicine* **2010**, *5*, 233–242, doi:10.2217/nnm.09.106.
- 1288 91. Schmitt, R.; Nenning, A.; Kraynis, O.; Korobko, R.; Frenkel, A.I.; Lubomirsky, I.; Haile, S.M.; Rupp,
1289 J.L.M. A Review of Defect Structure and Chemistry in Ceria and Its Solid Solutions. *Chem Soc Rev*
1290 **2020**, *49*, 554–592, doi:10.1039/C9CS00588A.
- 1291 92. Luo, S.; Li, M.; Fung, V.; Sumpter, B.G.; Liu, J.; Wu, Z.; Page, K. New Insights into the Bulk and Surface
1292 Defect Structures of Ceria Nanocrystals from Neutron Scattering Study. *Chemistry of Materials* **2021**,
1293 *33*, 3959–3970, doi:10.1021/acs.chemmater.1c00156.
- 1294 93. Bao, H.; Qian, K.; Fang, J.; Huang, W. Fe-Doped CeO₂ Solid Solutions: Substituting-Site Doping versus
1295 Interstitial-Site Doping, Bulk Doping versus Surface Doping. *Appl Surf Sci* **2017**, *414*, 131–139,
1296 doi:10.1016/j.apsusc.2017.04.018.
- 1297 94. Li, G.; Smith, R.L.; Inomata, H. Synthesis of Nanoscale Ce_{1-x}Fe_xO₂ Solid Solutions via a Low-
1298 Temperature Approach. *J Am Chem Soc* **2001**, doi:10.1021/ja016502.
- 1299 95. Zhao, B.; Shao, Q.; Hao, L.; Zhang, L.; Liu, Z.; Zhang, B.; Ge, S.; Guo, Z. Yeast-Template Synthesized
1300 Fe-Doped Cerium Oxide Hollow Microspheres for Visible Photodegradation of Acid Orange 7. *J*
1301 *Colloid Interface Sci* **2018**, *511*, 39–47, doi:10.1016/j.jcis.2017.09.077.
- 1302 96. Bao, H.; Chen, X.; Fang, J.; Jiang, Z.; Huang, W. Structure-Activity Relation of Fe₂O₃–CeO₂ Composite
1303 Catalysts in CO Oxidation. *Catal Letters* **2008**, *125*, 160–167, doi:10.1007/s10562-008-9540-3.

- 1304 97. Liu, H.; Wu, Y.; Liu, L.; Chu, B.; Qin, Z.; Jin, G.; Tong, Z.; Dong, L.; Li, B. Three-Dimensionally Ordered
1305 Macroporous Fe-Doped Ceria Catalyst with Enhanced Activity at a Wide Operating Temperature
1306 Window for Selective Catalytic Reduction of NO_x. *Appl Surf Sci* **2019**, *498*, 143780,
1307 doi:10.1016/j.apsusc.2019.143780.
- 1308 98. Aragón, F.F.H.; Aquino, J.C.R.; Ramos, J.E.; Coaquira, J.A.H.; Gonzalez, I.; Macedo, W.A.A.; da Silva,
1309 S.W.; Morais, P.C. Fe-Doping Effects on the Structural, Vibrational, Magnetic, and Electronic
1310 Properties of Ceria Nanoparticles. *J Appl Phys* **2017**, *122*, doi:10.1063/1.4999457.
- 1311 99. Martínez-Arias, A.; Fernández-García, M.; Salamanca, L.N.; Valenzuela, R.X.; Conesa, J.C.; Soria, J.
1312 Structural and Redox Properties of Ceria in Alumina-Supported Ceria Catalyst Supports. *J Phys Chem*
1313 *B* **2000**, *104*, 4038–4046, doi:10.1021/jp992796y.
- 1314 100. SCHWIDDER, M.; KUMAR, M.; KLEMENTIEV, K.; POHL, M.; BRUCKNER, A.; GRUNERT, W. Selective
1315 Reduction of NO with Fe-ZSM-5 Catalysts of Low Fe Content. I. Relations between Active Site
1316 Structure and Catalytic Performance. *J Catal* **2005**, *231*, 314–330, doi:10.1016/j.jcat.2005.01.031.
- 1317 101. Shafia, E.; Esposito, S.; Manzoli, M.; Chiesa, M.; Tiberto, P.; Barrera, G.; Menard, G.; Allia, P.; Freyria,
1318 F.S.; Garrone, E.; et al. Al/Fe Isomorphic Substitution versus Fe₂O₃ Clusters Formation in Fe-Doped
1319 Aluminosilicate Nanotubes (Imogolite). *Journal of Nanoparticle Research* **2015**, *17*, 336,
1320 doi:10.1007/s11051-015-3130-2.
- 1321 102. Katta, L.; Thrimurthulu, G.; Reddy, B.M.; Muhler, M.; Grünert, W. Structural Characteristics and
1322 Catalytic Performance of Alumina-Supported Nanosized Ceria–Lanthana Solid Solutions. *Catal Sci*
1323 *Technol* **2011**, *1*, 1645, doi:10.1039/c1cy00312g.
- 1324 103. Makuła, P.; Pacia, M.; Macyk, W. How To Correctly Determine the Band Gap Energy of Modified
1325 Semiconductor Photocatalysts Based on UV–Vis Spectra. *J Phys Chem Lett* **2018**, *9*, 6814–6817,
1326 doi:10.1021/acs.jpclett.8b02892.
- 1327 104. George, S.; Pokhrel, S.; Ji, Z.; Henderson, B.L.; Xia, T.; Li, L.; Zink, J.I.; Nel, A.E.; Mädler, L. Role of Fe
1328 Doping in Tuning the Band Gap of TiO₂ for the Photo-Oxidation-Induced Cytotoxicity Paradigm. *J Am*
1329 *Chem Soc* **2011**, *133*, 11270–11278, doi:10.1021/ja202836s.
- 1330 105. El-Hagary, M.; Shaaban, E.R.; Moustafa, S.H.; Gad, G.M.A. The Particle Size-Dependent Optical Band
1331 Gap and Magnetic Properties of Fe-Doped CeO₂ Nanoparticles. *Solid State Sci* **2019**, *91*, 15–22,
1332 doi:10.1016/j.solidstatesciences.2019.03.005.
- 1333 106. Dhannia, T.; Jayalekshmi, S.; Santhosh Kumar, M.C.; Prasada Rao, T.; Chandra Bose, A. Effect of Iron
1334 Doping and Annealing on Structural and Optical Properties of Cerium Oxide Nanocrystals. *Journal of*
1335 *Physics and Chemistry of Solids* **2010**, *71*, 1020–1025, doi:10.1016/j.jpcs.2010.04.011.
- 1336 107. Yang, H.; Jia, L.; Zhang, Z.; Xu, B.; Zhang, Q.; Yuan, S.; Xiao, Y.; Nan, Z.; Zhang, M.; Zhang, Y.; et al.
1337 Enhanced Photocatalytic VOCs Degradation Performance on Fe-Doped Ceria under Visible Light.
1338 *Appl Mater Today* **2022**, *29*, 101651, doi:10.1016/j.apmt.2022.101651.
- 1339 108. Spanier, J.E.; Robinson, R.D.; Zhang, F.; Chan, S.-W.; Herman, I.P. Size-Dependent Properties
1340 of CeO₂-y Nanoparticles as Studied by Raman Scattering. *Phys Rev B* **2001**, *64*, 245407,
1341 doi:10.1103/PhysRevB.64.245407.
- 1342 109. Wu, Z.; Li, M.; Howe, J.; Meyer, H.M.; Overbury, S.H. Probing Defect Sites on CeO₂ Nanocrystals with
1343 Well-Defined Surface Planes by Raman Spectroscopy and O₂ Adsorption. *Langmuir* **2010**, *26*, 16595–
1344 16606, doi:10.1021/la101723w.

- 1345 110. Dohčević-Mitrović, Z.D.; Šćepanović, M.J.; Grujić-Brojčin, M.U.; Popović, Z.V.; Bošković, S.B.;
 1346 Matović, B.M.; Zinkevich, M.V.; Aldinger, F. The Size and Strain Effects on the Raman Spectra of
 1347 Ce_{1-x}Nd_xO_{2-δ} (0 ≤ x ≤ 0.25) Nanopowders. *Solid State Commun* **2006**, *137*, 387–390,
 1348 doi:10.1016/j.ssc.2005.12.006.
- 1349 111. Popović, Z. V.; Dohčević-Mitrović, Z.D.; Paunović, N.; Radović, M. Evidence of Charge Delocalization
 1350 in Ce_{1-x}Fe_xO₂ + (3 + y) O₂ - y Nanocrystals (x = 0, 0.06, 0.12). *Phys Rev B* **2012**, *85*, 014302,
 1351 doi:10.1103/PhysRevB.85.014302.
- 1352 112. Nakajima, A.; Yoshihara, A.; Ishigame, M. Defect-Induced Raman Spectra in Doped CeO_2/Mn
 1353 CeO_2/Mn . *Phys Rev B* **1994**, *50*, 13297–13307,
 1354 doi:10.1103/PhysRevB.50.13297.
- 1356 113. Gallucci, N.; Hmoudah, M.; Martinez, E.; El-Qanni, A.; Di Serio, M.; Paduano, L.; Vitiello, G.; Russo, V.
 1357 Photodegradation of Ibuprofen Using CeO₂ Nanostructured Materials: Reaction Kinetics, Modeling,
 1358 and Thermodynamics. *J Environ Chem Eng* **2022**, *10*, 107866, doi:10.1016/j.jece.2022.107866.
- 1359 114. Paparazzo, E. Use and Mis-Use of x-Ray Photoemission Spectroscopy Ce_{3d} Spectra of Ce₂O₃ and
 1360 CeO₂. *Journal of Physics: Condensed Matter* **2018**, *30*, 343003, doi:10.1088/1361-648X/aad248.
- 1361 115. Romeo, M.; Bak, K.; El Fallah, J.; Le Normand, F.; Hilaire, L. XPS Study of the Reduction of Cerium
 1362 Dioxide. *Surface and Interface Analysis* **1993**, *20*, 508–512, doi:10.1002/sia.740200604.
- 1363 116. Idriss, H. On the Wrong Assignment of the XPS O1s Signal at 531–532 EV Attributed to Oxygen
 1364 Vacancies in Photo- and Electro-Catalysts for Water Splitting and Other Materials Applications. *Surf*
 1365 *Sci* **2021**, *712*, 121894, doi:10.1016/j.susc.2021.121894.
- 1366 117. Cardenas, L.; Molinet-Chinaglia, C.; Loridant, S. Unraveling Ce³⁺ Detection at the Surface of Ceria
 1367 Nanopowders by UPS Analysis. *Physical Chemistry Chemical Physics* **2022**, *24*, 22815–22822,
 1368 doi:10.1039/D2CP02736D.
- 1369 118. Liu, T.; Guo, L.; Tao, Y.; Hu, T.D.; Xie, Y.N.; Zhang, J. Bondlength Alternation of Nanoparticles Fe₂O₃
 1370 Coated with Organic Surfactants Probed by EXAFS. *Nanostructured Materials* **1999**, *11*, 1329–1334,
 1371 doi:10.1016/S0965-9773(99)00425-0.
- 1372 119. Turco, R.; Bonelli, B.; Armandi, M.; Spiridigliozzi, L.; Dell'Agli, G.; Deorsola, F.A.; Esposito, S.; Di Serio,
 1373 M. Active and Stable Ceria-Zirconia Supported Molybdenum Oxide Catalysts for Cyclooctene
 1374 Epoxidation: Effect of the Preparation Procedure. *Catal Today* **2020**, *345*, 201–212,
 1375 doi:10.1016/j.cattod.2019.10.036.
- 1376 120. Wang, Y.; Wang, F.; Song, Q.; Xin, Q.; Xu, S.; Xu, J. Heterogeneous Ceria Catalyst with Water-Tolerant
 1377 Lewis Acidic Sites for One-Pot Synthesis of 1,3-Diols via Prins Condensation and Hydrolysis
 1378 Reactions. *J Am Chem Soc* **2013**, *135*, 1506–1515, doi:10.1021/ja310498c.
- 1379 121. Rebellato, J.; Natile, M.M.; Glisenti, A. Influence of the Synthesis Procedure on the Properties and
 1380 Reactivity of Nanostructured Ceria Powders. *Appl Catal A Gen* **2008**, *339*, 108–120,
 1381 doi:10.1016/j.apcata.2007.12.031.
- 1382 122. Badri, A.; Binet, C.; Lavalley, J.-C. An FTIR Study of Surface Ceria Hydroxy Groups during a Redox
 1383 Process with H₂. *Journal of the Chemical Society, Faraday Transactions* **1996**, *92*, 4669,
 1384 doi:10.1039/ft9969204669.

- 1385 123. Natile, M.M.; Boccaletti, G.; Glisenti, A. Properties and Reactivity of Nanostructured CeO₂
 1386 Powders: Comparison among Two Synthesis Procedures. *Chemistry of Materials* **2005**, *17*, 6272–
 1387 6286, doi:10.1021/cm051352d.
- 1388 124. Matussin, S.N.; Khan, F.; Harunsani, M.H.; Kim, Y.-M.; Khan, M.M. Visible-Light-Induced
 1389 Photocatalytic and Photoantibacterial Activities of Co-Doped CeO₂. *ACS Omega* **2023**, *8*, 11868–
 1390 11879, doi:10.1021/acsomega.2c07058.
- 1391 125. Xu, B.; Yang, H.; Zhang, Q.; Yuan, S.; Xie, A.; Zhang, M.; Ohno, T. Design and Synthesis of Sm, Y, La
 1392 and Nd-doped CeO₂ with a Broom-like Hierarchical Structure: A Photocatalyst with Enhanced
 1393 Oxidation Performance. *ChemCatChem* **2020**, *12*, 2638–2646, doi:10.1002/cctc.201902309.
- 1394 126. Zdanowicz, T.; Rodziejewicz, T.; Zabkowska-Waclawek, M. Theoretical Analysis of the Optimum Energy
 1395 Band Gap of Semiconductors for Fabrication of Solar Cells for Applications in Higher Latitudes
 1396 Locations. *Solar Energy Materials and Solar Cells* **2005**, *87*, 757–769,
 1397 doi:10.1016/j.solmat.2004.07.049.
- 1398 127. Rao, Y.; Xue, D.; Pan, H.; Feng, J.; Li, Y. Degradation of Ibuprofen by a Synergistic UV/Fe(III)/Oxone
 1399 Process. *Chemical Engineering Journal* **2016**, *283*, 65–75, doi:10.1016/j.cej.2015.07.057.

1400

1401

1402 Highlights

- 1403 • Reverse micelle synthesis fosters Fe doping of nanocrystalline CeO₂
 1404 • 2.5 mol % iron-doped ceria leads to high charge delocalization
 1405 • Efficient visible-light photodegradation of ibuprofen with 2.5 mol % Fe-CeO₂
 1406 • Substitutional Fe favours the oxygen vacancies formation and ibuprofen adsorption.
 1407 • The by-product of the ibuprofen degradation is 1-ethenyl-4-(2-methylpropyl)benzene.

1408

1409